

CHARACTERIZATION OF A NONINVASIVE, *IN VIVO*, MICROSCOPIC
HYPERSPETRAL IMAGING SYSTEM FOR
MICROVASCULAR VISUALIZATION

By

BHAVESH SHAH

Presented to the Faculty of the Graduate School of
The University of Texas at Arlington in Partial Fulfillment
of the Requirements
for the Degree of

MASTER OF SCIENCE IN BIOMEDICAL ENGINEERING

THE UNIVERSITY OF TEXAS AT ARLINGTON

May 2006

Copyright © by Bhavesh Shah 2006

All Rights Reserved

ACKNOWLEDGEMENTS

I would like to take a moment, to convey my gratitude to all those people who have helped me complete this master's thesis.

Firstly, I am profoundly indebted to my supervisor and mentor Dr. Karel Zuzak, for his unconditional support and encouragement. Dr. Zuzak was always present to listen and to give advice. He has educated me with various aspects in research, and the need to be persistent to accomplish my goals. It forever will remain my pleasure to have worked with Dr. Zuzak.

I am grateful towards Dr. Khosrow Behbehani, advisor and chair to the Biomedical Engineering department at UTA, for accepting the invitation to be one of the committee members and for his guidance on all research matters and innumerable academic counseling. I am very grateful towards Dr. Doyle Hawkins, Associate Chair of Mathematics Department at UTA, for being part of the committee and statistical aid in thesis matters. A special note of thank to Dr. Cavanagh, Vice Chairman Dept. of Ophthalmology at UT southwestern, and Dr. Patrol, Professor at UT southwestern, for their professional advice without which this effort wouldn't be successful.

I am very thankful towards my fellow friends and lab mates Amogh Kothare, Prasad Gundabhat and Nirad Zinzuwadia for their key suggestions and discussions.

At the end, I would and will ever remain thankful towards my beloved parents, my brother, sister-in-law for showering their support and love in all my endeavors here and henceforth.

April 18, 2006

ABSTRACT

CHARACTERIZATION OF A NONINVASIVE, *IN VIVO*, MICROSCOPIC HYPERSPETRAL IMAGING SYSTEM FOR MICROVASCULAR VISUALIZATION

Publication No. _____

Bhavesh Shah, M.S.

The University of Texas at Arlington, 2006

Supervising Professor: Karel Zuzak

Instrumentation with clinical implications for imaging the human oculus was developed, based upon the hyperspectral imaging modality. The novel, non invasive, microscopic multi-modal hyperspectral imaging system, which operates in the visible as well as near infrared region, is capable of generating images illustrating spatial distribution of oxyhemoglobin contributions. The device principally comprises of a liquid crystal tunable filter and a focal plane array detector that is integrated to the slit lamp microscope. A proof of principle clinical study involving ten healthy subjects was undertaken to image the microvascular structure within the dermal tissue within the near

infrared region, however these results are not validated. The spectral range used in the study was 650 – 1050nm, with a spectral resolution of 5nm, magnification of 10X to obtain a 35 ms acquisition time and a spatial resolution of 0.054 mm at binning of 1 x 1. The successful dermal microvascular study paved way for imaging the human eye using the visible region, wherein the anterior scleral surface was visualized in seven healthy subjects to spatially map the oxyhemoglobin contributions in the microvasculature perfusing the sclera. The spectral range used in the human eye study was 520 – 602nm, with a spectral resolution of 2nm, magnification of 10X to obtain a 5 ms acquisition time and a spatial resolution of 0.038 mm at binning of 2 x 2.

TABLE OF CONTENTS

ACKNOWLEDGEMENTS.....	iii
ABSTRACT.....	v
LIST OF ILLUSTRATIONS.....	x
LIST OF TABLES.....	xiii
Chapter	
1. INTRODUCTION.....	1
1.1 Hyperspectral Imaging	1
1.2 Hyperspectral Imaging : Cuvette Example.....	3
1.3 Hemoglobin and its Derivatives.....	5
1.3.1 Oxyhemoglobin.....	6
1.4 Research Problem.....	7
2. METHODS.....	8
2.1 Instrument.....	8
2.1.1 Slit Lamp.....	10
2.1.2 Relay Optics.....	12
2.1.3 Liquid Crystal Tunable Filter.....	13
2.1.4 LCTF Operating Consideration.....	17

2.1.4.1	Variation of FWHM with Pass Wavelength.....	17
2.1.4.2	Response time Versus Tuning Wavelength.....	18
2.1.4.3	Thermal Drift and Re-initialization.....	18
2.1.4.4	Response times versus Temperature.....	18
2.1.5	Camera Lens.....	18
2.1.6	Focal Plane Array (FPA).....	19
2.1.6.1	PIXIS: 400BR.....	20
2.1.6.2	CoolSNAP _{ES}	24
2.1.6.3	Binning.....	27
2.2	Experimental Section	31
2.2.1	Reference Spectra	31
2.2.2	Experiment Protocol	33
2.2.3	Data Acquisition	34
2.2.4	Determination of Experimental parameters.....	37
2.2.5	Data Analysis	41
3.	RESULTS.....	44
3.1	System Characterization.....	44
3.1.1	Slit Lamp Source.....	44
3.1.2	LCTF Calibration.....	47
3.1.3	FPA Calibration.....	54
3.2	System Performance.....	62
4.	DISCUSSION	68

4.1. Microscopic Near Infrared Hyperspectral Imaging system	68
4.2. Microscopic Visible Hyperspectral Imaging system	71
5. CONCLUSIONS AND FUTURE GOALS	73
APPENDIX	
A. UTA SUBJECT CONSENT FORM – DERMAL.....	74
B. UTA SUBJECT CONSENT FORM - HUMAN EYE.....	79
REFERENCES.....	84
BIOGRAPHICAL INFORMATION.....	90

LIST OF ILLUSTRATIONS

Figure		Page
1.	Hyperspectral Data Cube Visualization. A) Depicts sequence of images acquired at specific desired wavelengths. B) Depicts Spectral information obtained from each pixel over the stack of images	2
2.	Cuvette Experiment demonstrating Characteristics of a Hyperspectral Imaging system	4
3.	Structure of Hemoglobin Molecule	5
4.	Pictorial presentation of the Microscopic Near Infrared Hyperspectral Imaging system	9
5.	Pictorial presentation of the Microscopic Visible Hyperspectral Imaging system	10
6.	Marco G2 Slit Lamp Picture	11
7.	Schematic diagram of an LCTF stage	13
8.	Side view schematic representation of alignment of liquid crystals in the presence of Electric field	14
9.	Liquid Crystal Tunable Filter Module Picture	15
10.	60 mm,F/2.8D AF Micro-Nikkor lens	19
11.	PIXIS: 400BR Focal plane Array Picture	21
12.	Spectral response for PIXIS: 400BR FPA adopted from Photometrics,Inc ..	23
13.	CoolSNAP _{ES} CCD Image	25
14.	Spectral response of the CoolSNAP _{ES} CCD adopted from Photometrics, Inc	24

15. Frame readout, binning 1 x 1	28
16. Frame readout, binning 2 x 2	29
17. Formation of Superpixels, binning 2 x 2	30
18. Formation of Superpixels, binning 3 x 3	30
19. Formation of Superpixels, binning 4 x 4	31
20. Reference Spectra for Oxyhemoglobin and Deoxyhemoglobin within Visible region	32
21. Reference Spectra for oxyhemoglobin and Deoxyhemoglobin within the Near Infrared region	33
22. Experimental setup for the Clinical Study	35
23. Output spectrum for the Near infrared microscopic hyperspectral system ...	39
24. Output spectrum for the Visible microscopic hyperspectral system	40
25. Slit Lamp Source Intensity Versus Distance	45
26. Comparison of average temperature variations over a period of 30 seconds with the Source Off and Source On	46
27. Near Infrared LCTF calibration curve with the dash line indicating the regressed line	48
28. Visible Low resolution LCTF calibration curve experimental setup	49
29. Visible low resolution LCTF calibration curve.	49
30. Spectral Band-pass plot for Near Infrared LCTF	50
31. Spectral Band-pass plot for Visible low resolution LCTF	51
32. Tune-Delay/Tunewait time experimental setup	52

33. NIR LCTF Tune-Delay time experimental outcome	53
34. Visible LCTF Tune-delay time experimental result	54
35. A) .1951 USAF resolution target. (B) Reflected Intensity plotted for the dotted line in (A)	55
36. Spatial resolving power plot versus Percent contrast for PIXIS: 400BR FPA and slit lamp magnification 10X	57
37. Spatial resolving power plot versus Percent contrast for PIXIS: 400BR FPA and slit lamp magnification 16X	57
38. Spatial Resolution plot as a function of Percent contrast for PIXIS: 400BR FPA lamp and slit magnification 25X	58
39. Spatial resolving power plot versus Percent contrast for CoolSNAP _{ES} FPA and slit lamp magnification 10X	59
40. Spatial resolving power plot versus Percent contrast for CoolSNAP _{ES} FPA and slit lamp magnification 10X without the relay optics in the light path ..	60
41. Image Alignment. A) Image off centre from the CCD chip. B) Visually aligned imaged onto the center of the CCD chip	61
42. Near infrared Hyperspectral imaging. A) Gray scale encoded image depicting oxyhemoglobin contribution. B) Spectral output averaged over area under the Boxes	63
43. Near infrared Hyperspectral imaging. A) Gray scale encoded image visualized as oxyhemoglobin contribution. B) Spectral output averaged over the region under the boxes	63
44. Microscopic hyperspectral imaging of the eye. A) Color encoded image showing oxyhemoglobin contribution values as a function of space. B) Spectral analysis from the pink box region resembling deoxyhemoglobin reference curve C) Spectral output over the black box region resembling strong oxyhemoglobin reference curve.....	65

LIST OF TABLES

Table	Page
1. Specifications for the Visible low resolution LCTF.....	17
2. Specifications of Near Infrared LCTF	17
3. Specifications of PIXIS: 400BR camera.....	20
4. Specifications chart for CoolSNAP _{ES}	24
5. Oxyhemoglobin contributions in Dermal tissue microvasculature.....	64
6. Oxyhemoglobin contributions in Scleral surface microvasculature.....	66

CHAPTER 1

INTRODUCTION

1.1 Hyperspectral Imaging

NASA's pioneering techniques integrating spatial and spectral imaging methods for its remote sensing technology developed for Earth resources monitoring, led the way for the development of Hyperspectral imaging in the field of medicine [1]. Hyperspectral Imaging is an optical imaging technique that captures the spatial and spectral information from the source target, typically capturing hundreds, of contiguous wavelength bands for each pixel. The hyperspectral data would be rendered useless, until the recorded data is precisely analyzed and processed using tools borrowed from spatial image processing, chemometrics and spectroscopy to yield information that can be presented in an image form [1]. Thus the Hyperspectral imaging approach provides a "data cube" consisting of two dimensional images with each desired wavelength being represented by one of the images from the stack of images collected [2]. The image cube thus obtained, has three dimensions: 2 spatial (X and Y) and 1 spectral dimension (wavelength) [3]. A basic hyperspectral imaging system consists of a broadband light source, with the desired spectral band of interest; that focuses light on the source target,

an electronically tunable filter to spectrally discriminate the imaged light from the source target and a sensitive array detector, focal plane array, which collects the light, converts it into two dimensional gray scaled image and transfers it to a computer. The image acquisition process continues until all images at desired wavelength have been collected, generating the hyperspectral image cube. An overview of a Hyperspectral image cube is depicted in Figure 1, **A** shows the sequence of images acquired simultaneously at different wavelength bands. The corresponding intensity values for a particular pixel taken along the series of image planes plotted as a function of wavelength is depicted in **B**.

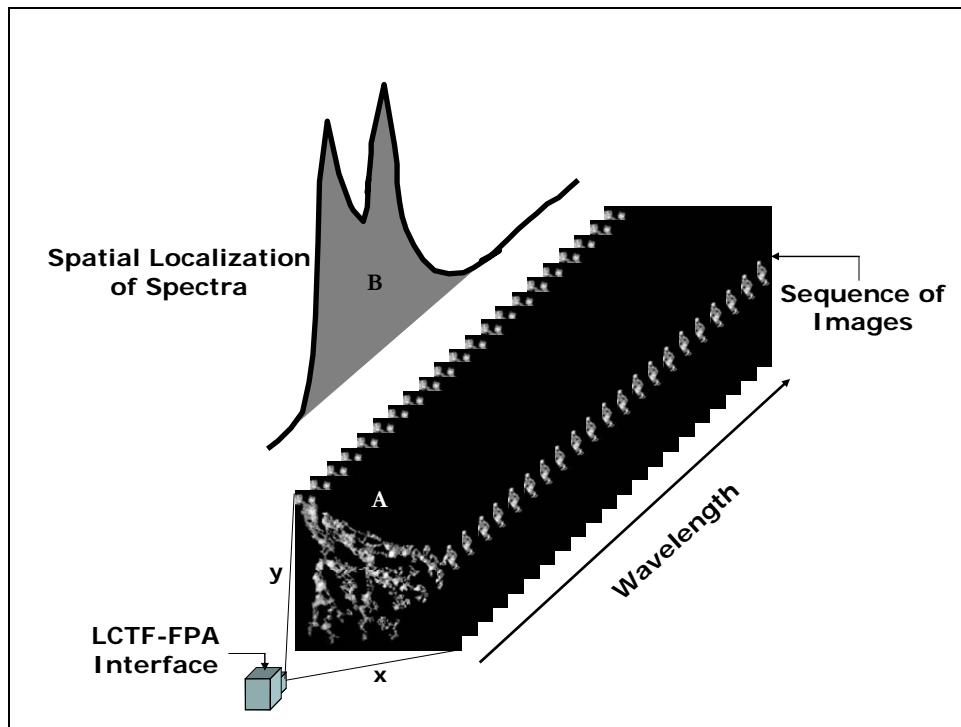


Figure 1, Hyperspectral Data Cube Visualization. **A**) Depicts sequence of images acquired at specific desired wavelengths. **B**) Depicts Spectral information obtained from each pixel over the stack of images.

Hyperspectral imager components with improved spectral and spatial resolution provide high optical precision can be used to provide medical diagnosis without relying on the clinical examination skills of the physicians. Besides the diagnosis is relatively non-invasive, i.e. there is no need to perform a biopsy in cases such as cervical neoplasia, tumours etc. indicating less pain to the patient, and a relatively low cost diagnosis which takes place in real time.

Real time information can be most important during surgery where hyperspectral imagery can serve as a visual aid to the surgeons. Hyperspectral applications are being developed that look deeper than the blood drenched operative field saving critical time that is invested by the surgeon in clearing the blood. Also applications are being developed which aid surgeon in better distinguishing organs in and around the operative field minimizing the errors in surgery which occur due to the similar color of the organs [6].

Hyperspectral technology provides digital images of the sub-cellular morphology to a good precision many image processing algorithm in conjunction with the spectral signatures of various components, quantitative information can be extracted from the target imaged. This information could well be important for early diagnosis of a disease state or assist in patient care.

1.2 Hyperspectral Imaging : Cuvette Example

As an example, an experiment was performed to demonstrate the characteristics and capabilities the microscopic hyperspectral imaging system. In this experiment we imaged two cuvettes in the light path, one filled with air and other with water, within

the wavelength range 650 – 1050 nm. Spectral information from a small region in an analyzed hyperspectral cube from both the cuvettes was plotted, Figure 2.

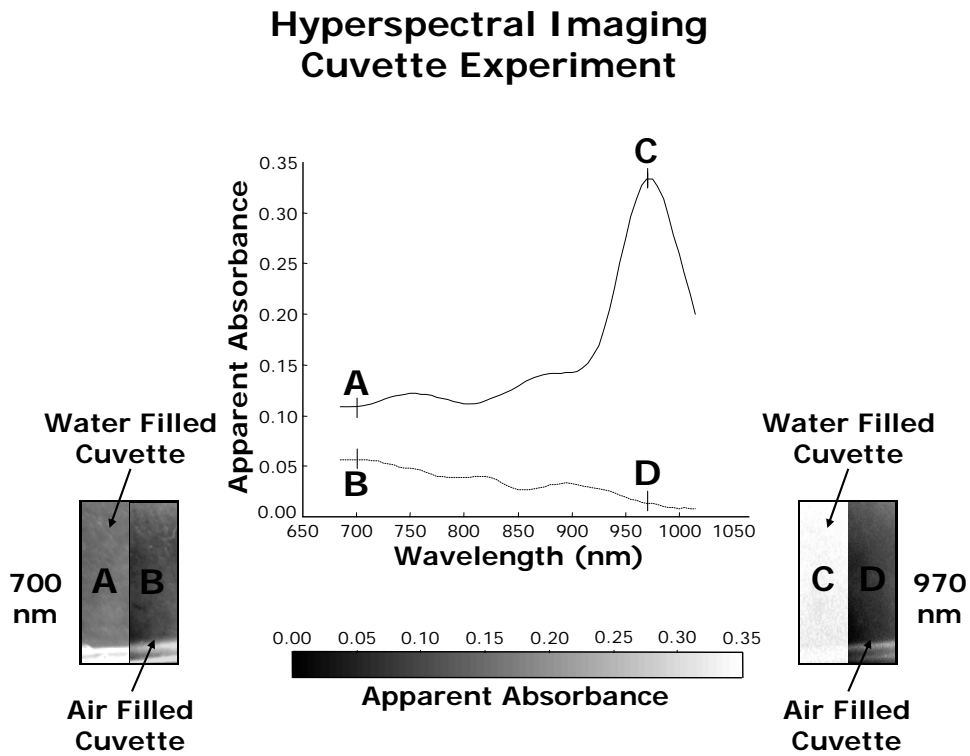


Figure 2, Cuvette Experiment demonstrating Characteristics of a Hyperspectral Imaging system.

The solid line displays the plot from the cuvette filled with water and it distinctly represents water absorption spectrum [7]. Further two images were pulled out from the analyzed data for the cuvettes at 700nm and 970nm showing the progression that as water absorbs more light (absorption peak being near 970nm), with increasing wavelength the image becomes brighter displaying the trend that brighter the image more is the absorption by the substance in the illumination path. Thus this cuvette

experiment provides us with significant evidence of the spectral (Graph, Figure 2) and spatial (Images, Figure 2) differentiation of the hyperspectral imaging system.

1.3 Hemoglobin and its Derivatives

Hemoglobin, an integral part of the Erythrocyte or Red blood cell (RBC) is produced in the bone marrow [8]. An average adult containing about 5 liters of blood has about 5 billion RBC's/mililiter of blood and each RBC normally enclose about 280 million hemoglobin molecules adding unto totally 790 grams of hemoglobin [9]. It is imperative to maintain strict hemoglobin amounts since increase or decrease within them is long been related to anemia, Kidney diseases, congenital heart problems, pulmonary fibrosis etc. [10]

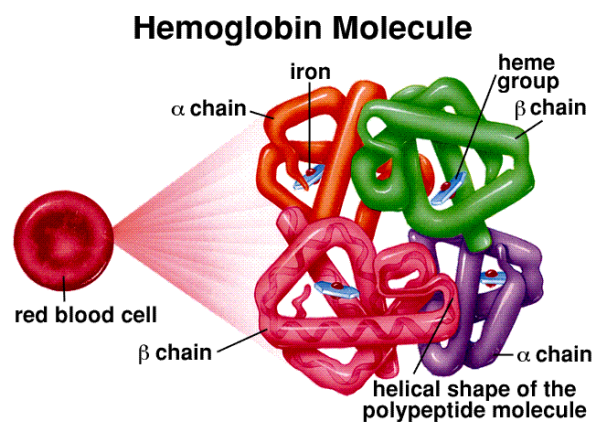


Figure 3, Structure of Hemoglobin Molecule. [11]

Hemoglobin molecule is a tetramer protein containing totally four chains – two similar chains labeled as α , with 141 amino acids and rest two identical chains labeled as β , with 146 amino acids, Figure 3 [12]. The adjacent monomers are interlinked via hydrophobic links and comprised of a heme group (reduced form) rooted within a globin [13]. Hemoglobin's primary function is to bind oxygen that diffuses into the bloodstream from the lungs and then transport it to outlying tissues where it is released primarily for aerobic respiration [9]. Besides being oxygen carrier, hemoglobin replenishes Myoglobin, a protein functioning as "oxygen stores" for the muscles [9].

A hemoglobin molecule contain 4 heme groups, each of which can bind at least one oxygen molecule thus, a hemoglobin molecule can bind between 1 and 4 O_2 molecules, ranging from fully "desaturated" hemoglobin (deoxyHb) to fully "saturated" hemoglobin (oxyHb). The molecule functions by absorbing oxygen where the oxygen tension is high (Lungs) and releasing oxygen where the tension is low (Tissue). The oxygen-hemoglobin dissociation curve is sigmoidal suggesting *cooperative binding* between them meaning one oxygen molecule causes the next oxygen molecule to bind more strongly, the third oxygen even more strongly and so on [12].

1.3.1 Oxyhemoglobin

Oxyhemoglobin, a bright red compound, is an inherent blood chromophore formed during respiration when oxygen molecule binds to hemoglobin, found in erythrocytes. The process of oxyhemoglobin formation takes place in the lungs (alveoli) where the partial pressure of oxygen is high. This compound then travels through the

vascular conduits and delivers oxygen to the cells, where the partial pressure of oxygen is less, in exchange of carbon dioxide. Oxyhemoglobin has a specific absorption characteristic of light with peaks at 540nm & 576nm in the visible region and 940nm in Near-Infrared region [7,14].

1.4 Research Problem

The aspiration of this research endeavor is to assemble a microscopic multi-modal reflectance hyperspectral imaging system which is capable of visualizing relative contributions of Oxyhemoglobin for clinical applications in the Visible and near infrared region. Once assembling the system is accomplished, the next task is to characterize individual components of the imaging system that include the slit lamp source, the LCTF and the Focal plane array. Further, the research path is to image the microvascular structure within the dermal tissue of the palmar region employing a clinical study and provide evidence to the fact that the system is capable of measuring oxyhemoglobin contributions and generate images that have spatial distributions of oxyhemoglobin contributions. Once all the above processes are determined to be satisfactory, clinical application towards imaging the Sclera of the human eye will be undertaken.

CHAPTER 2

METHODS

2.1 Instrument

The multi-modal microscopic reflectance Hyperspectral Imaging system developed at UTA in the Laboratory of Biomedical Imaging is envisioned to provide enhanced diagnosis in a clinical environment. The system developed has the capability to measure relative contributions of Oxyhemoglobin in the microvasculature in the visible as well as the near infrared region, hence multi-modal. A proof of principle study was formulated to measure contributions of oxyhemoglobin in the microvasculature perfusing the dermal tissue of the palm in the near infrared region. The system was also used to image the human eye measuring the relative contributions of oxyhemoglobin perfusing the scleral surface. The instrumentation used for this imaging system is shown in the Figure 4 and Figure 5.

The instrumentation shown below consists of a slit lamp that illuminates the target using an in-built 12V/30W illumination Halogen lamp source. The light from the source is focused onto the target which is placed on the Y-shaped headrest. The diffused reflected light from the target is passed back through the slit lamp microscope optics onto a beam splitters which allows a part of light into the Eyepiece for the observer and

the remaining part of light to the relay optics which further pass light into the LCTF, which is an electronically tunable filter discriminating the reflected light into individual wavelengths passing it onto the camera lens which then focuses it onto the Charged Coupled Device (CCD) camera. The images formed on the CCD are then digitized and stored in a Laptop computer for further analysis.

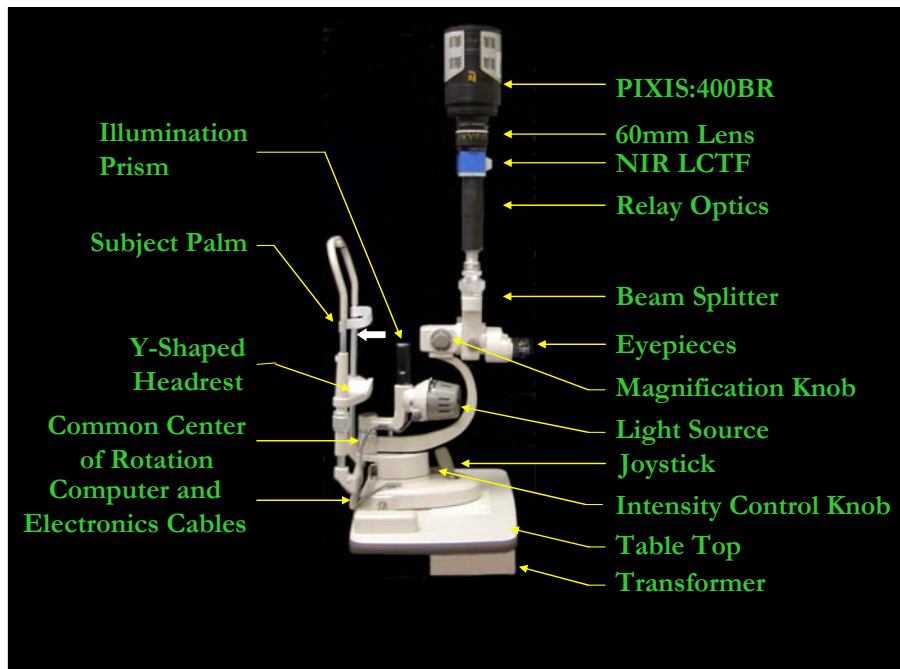


Figure 4, Pictorial presentation of the Microscopic Near Infrared Hyperspectral Imaging system.

Figure 4 displays the system which can be applied to collect data in the near infrared region whereas Figure 5 displays the system which is capable of collecting data in the visible region. The visible and near infrared application differ instrumentation wise from one another in the use of a different CCD camera, the COOLSNAP_{ES} camera

instead of the PIXIS camera and a different LCTF, visible LCTF instead of near infrared LCTF.

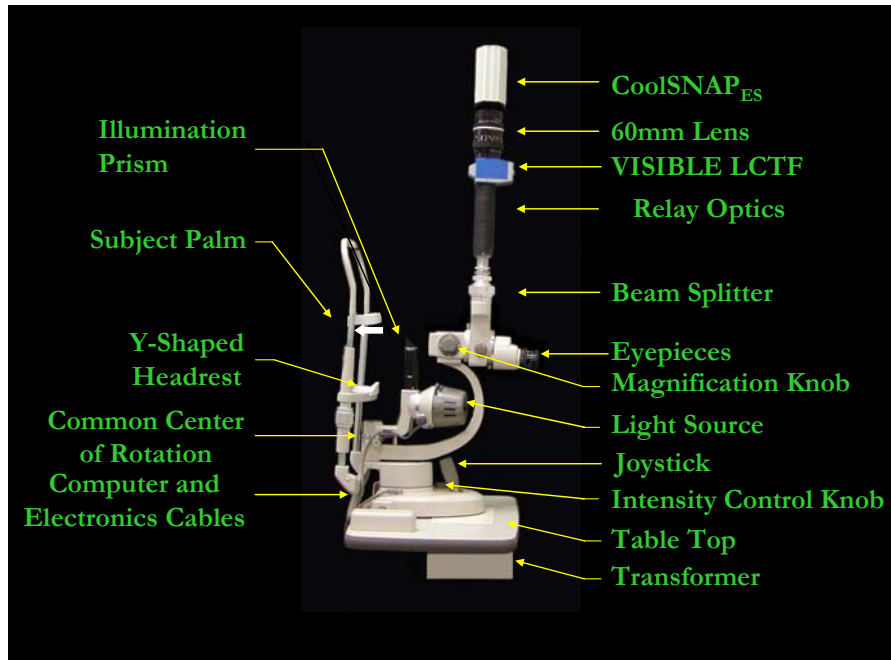


Figure 5, Pictorial presentation of the Microscopic Visible Hyperspectral Imaging system.

2.1.1 Slit Lamp

The slit lamp (Marco G2, Universal Ophthalmic Inc., Dallas, Texas) is a microscope comprised of an illumination system and an observation system, which are mounted on a rotated drum with a common centre of rotation [15]. The slit lamp, Figure 6, is binocular; that is, it has two eyepieces, giving the binocular observer a stereoscopic (three – dimensional) view of the eye, thus Biomicroscope as sometimes it is called [16, 17].



Figure 6, Marco G2 Slit Lamp Picture.

The microscope is mounted on a stage that is designed for precise and smoother movements of the microscope and positioning of the patient. Microscope position is controlled by an ergonomic joystick. Moving in and out allows the observer to focus the microscope at various depths. The joystick is also used to move the microscope side to side, allowing scanning and easy movement from one eye to another. Patient positioning is achieved by a standard Y-shaped head rest unit that includes a moveable chin rest and a stationary forehead band [18].

The Galilean magnification changer allows increasing the magnifying power between three stages i.e. 10X, 16X, 25X, by simply turning a knob which is designed with a flat area so that the operator can change the power by feel i.e. without looking at the markings since the higher magnification is achieved when flat portion is on top while lowers powers when the flat surface is at the bottom [18]. The actual magnification of what is seen through the slit lamp is derived by multiplying the power

of the eyepieces, which are fixed, with the power of the objective lens. Thus if the eyepieces are 10X and the objective lens is 1.6X, the total magnification is 16X [16, 17].

The light source of the slit lamp is a 12V/30W halogen lamp providing broadband white light. The light is controlled by a transformer which provides continuous light intensity with the help of rheostat placed next to the joystick. The slit width and the slit height can be continuously varied from 1-14mm [18].

A Beam splitter is effectively a semi-silvered mirror which is placed in-between the eyepiece and the microscope optics to partially transmit light to the eyepiece and partially reflect light to the attached CCD camera [15].

2.1.2 Relay Optics

Attaching the LCTF and the CCD camera onto the beam splitter of the slit lamp does not use a lot of CCD chip area i.e. the spot created by the reflected light from the slit lamp falling onto the CCD after passing through the LCTF is very small. Hence there arose a need to magnify the reflected light coming out of the beam splitter before passing onto the LCTF. Thus a relay optic module was designed which is composed of two optics namely Eyepiece and Photo eyepiece placed in a machined metal cylinder. Eyepiece lens is an optical system which is used to magnify images in optical instruments such as telescopes, microscopes etc. Photo eyepiece performs the function

of focusing the images onto a plane. These two optical components are housed in a metal cylinder 18 cm in length which was machined here in UTA.

2.1.3 Liquid Crystal Tunable Filter

The diffused reflectance light from the subjects palm passes through a Liquid Crystal Tunable Filter, LCTF, (Cambridge Research and Instrumentation [CRI], Woburn, MA) having solid-state construction and no-moving parts or vibrations, which works by applying voltage to its liquid crystal elements, to select a transmitted wavelength range, while blocking rest of the wavelengths. A feedback circuit associated with the LCTF grants it a stable and precise wavelength tuning continuously over hundreds of nanometers that is independent of ambient temperature within the range of 10° - 40° C [19,20].

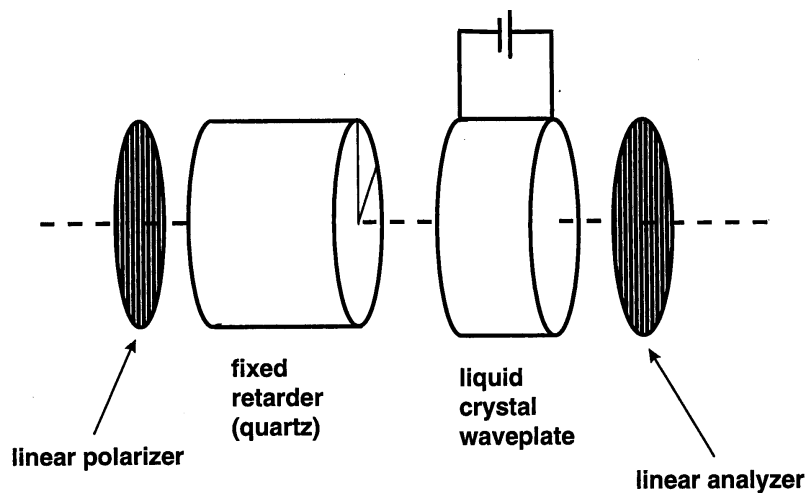


Figure 7, Schematic diagram of an LCTF stage. [21]

The LCTF, Figure 9, is comprised of several cascaded filter stages each consisting of a birefringent element (a fixed retarder), and Liquid crystal waveplate (an electronically controlled phase retarder) positioned between parallel linear polarizer as shown in Figure 7. Linearly polarized light passes through the birefringent element that introduces a phase difference dependent on the incident wavelength, birefringence of the material and the thickness of the material [22].

The liquid crystal waveplate consist of two transparent electrodes made up of indium-tin oxide placed on either side of the cell containing the nematic crystals that are aligned with their long axis nearly perpendicular to the light path., Figure 8. The inner surfaces of the liquid crystal cell are prepared in such a way that the molecules have a preferred orientation parallel to the surface. However, when a voltage is applied across the electrodes an electric field parallel to the light path is induced, generating a torque that is exerted, twisting the liquid crystals into the direction of electric field. As the molecules align more closely with the applied electric field, retardance through the liquid crystal waveplate decreases, producing an electronically adjustable retardance [21- 23].

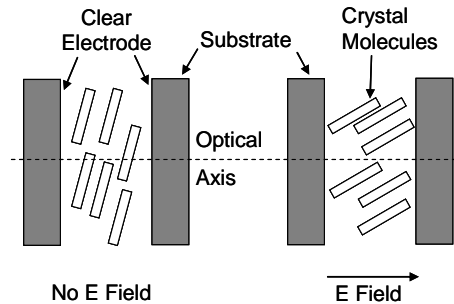


Figure 8, Side view schematic representation of alignment of liquid crystals in the presence of Electric field. [23]

The light passes through the linear analyzer (polarizer), which is parallel to incident or entry linear polarizer, and wavelengths of light which have undergone an integral phase shift through the combined fixed retarder and liquid crystal retarder are transmitted by the linear analyzer to the next filter stage. This yields a transmittance that is dependent on the phase shift which inherently depends on the total retardance offered by the fixed retarder and the Liquid crystal waveplate adjustable retarder. Thus to isolate light of wavelength λ , multiple retardance stages are placed in series, which allows the particular wavelength to be transmitted without loss, while light of other wavelengths is extinguished by one or more stages. The spectral range of the entire LCTF filter is determined by stage 1, the stage with the thinnest birefringent element. The bandpass of the device is dictated by the last stage, which comprises the thickest element [21-23].



Figure 9, Liquid Crystal Tunable Filter Module Picture.

The LCTF, Figure 9, consists of an Optics module and an Electronics module (controller box) that is used to drive the Optics module [24]. The host computer's USB interface provides complete control of the filter, using a series of ASCII commands and replies, and also powering the Electronics module. The required tunable wavelength is transmitted using the host computer HyperTerminal interface via the USB cable to the electronics module. The electronic module calculates the required voltage level (drive level) for each tunable element in the optics module for tuning the LCTF to the required wavelength [19, 20].

The response time, time to switch from one wavelength to another, depends on several factors including the liquid crystal relaxation time from "charge" to "no charge" states under various ambient temperatures and the calculation time of the electronics controller box, which must send the correct voltages to each liquid crystal element for each change. Typically, this time is 50ms to 150ms. An interesting thing to note about these filters is that its transmittance is sensitive to polarization of the input beam, and is increased by a factor of two if the input beam is polarized along the axis of the input polarizer [19, 20].

Some important specification for visible low resolution LCTF and the Near infrared LCTF used in the research are presented in the tables 1 & 2 below.

Table 1, Specifications for the Visible low resolution LCTF

Parameters	VariSpec VIS LCTF
Clear Aperture	20 mm
Bandwidth (FWHM)	4.5 – 12.5 nm
Field Of View (Half – Angle)	$\pm 7.5^\circ$ from normal
Wavelength range	400 – 720 nm
Wavelength accuracy	Bandwidth / 8
Optic Response Time	50
Operating Temperature	10° - 40° C

Table 2, Specifications of the Near infrared LCTF

Parameters	VariSpec SNIR LCTF
Clear Aperture	20 mm
Bandwidth (FWHM)	4.5 – 12.5 nm
Field Of View (Half – Angle)	$\pm 7.5^\circ$ from normal
Wavelength range	650 – 1100 nm
Wavelength accuracy	Bandwidth / 8
Optic Response Time	150
Operating Temperature	10° - 40° C

2.1.4 LCTF Operating Consideration

2.1.4.1 Variation of FWHM with Pass Wavelength

The Bandwidth is defined as how many adjacent wavelengths are transmitted at the full width of the curve at half the maximum transmission (FWHM). The FWHM

varies with wavelength as $1/8$, which being the intrinsic properties of all LYOT filters [25].

2.1.4.2 Response time Versus Tuning Wavelength

There is no simple relationship between the response time to change from one wavelength to another, and the wavelength involved, some wavelengths requests tune more LC elements than others, resulting in shorter or longer tuning speeds [25].

2.1.4.3 Thermal Drift and Re-initialization

The VariSpec filter has a slight drift when the optics module temperature changes resulting in a slight wavelength error. Performing the initialization routine renders the filter insensitive to temperature, to first order, and thus eliminates this error. If the ambient temperature changes by more than $\pm 3^\circ \text{C}$, it is wise to re-perform the initialization, otherwise the controller trips a flag which sends an error on the LED, thereby ceasing to tune [25].

2.1.4.4 Response time versus Temperature

The liquid crystal variable retarders set the response time of the filter, and their viscosity varies with the temperature. Higher the temperature lower is the viscosity; hence elevated temperature use is the single easiest way to improve the response speed. [25].

2.1.5 Camera Lens

The 60mm, F/2.8D micro-nikkor camera lens (Nikon, Melville, NY) focuses the light filtered by LCTF onto the CCD camera detector. It has the ability to produce

distortion-free images with superb resolution, sharpness and contrast. The lens has a good depth of field and a small working distance. The lens is shown below:



Figure 10, 60 mm,F/2.8D AF Micro-Nikkor lens.

The lens, Figure 8, has a number of F-stops which can be used to accordingly expose the camera CCD. The front side of the lens is used to adjust the focus on the image and the back side fits into a C-F mount which is used to couple the camera with the variable focus lens [26].

2.1.6 Focal Plane Array (FPA)

The charge coupled devices (CCD's) or FPA perform three essential functions: photons are transduced to electrons, integrated and stored, and finally read out. They can be roughly thought of a two-dimensional grid of individual photodiodes (called pixels), each connected to its own charge storage "well." Each pixel senses the intensity of light falling on its collection area, and stores a proportional amount of charge in its associated "well." Once charge accumulates for the specified exposure time, the time between start acquisition and stop acquisition, the pixels are read out serially [27].

2.1.6.1 PIXIS: 400BR

The Focal plane array used for near infrared region application a PIXIS: 400BR, from Princeton instruments (PIActon, Tuscon, Arizona).

Table 3, Specifications of PIXIS: 400BR camera.

Specifications	
CCD format	1340 x 400 imaging array 20 x 20- μ m pixels 26.0 x 8-mm imaging area
Well Capacity	300 Ke ⁻ , High sensitivity mode 1Me ⁻ , High Capacity mode
System Read noise	5 e ⁻ rms @ 100 KHz (Maximum) 16 e ⁻ rms @ 20 MHz (Maximum)
Nonlinearity	< 1% @ 100KHz, < 2% @ 2 MHz
Dynamic Range	16 bits
Frame readout	35 Hz @ 100KHz Digitization 74 Hz @ 2MHz Digitization
Deepest cooling Temperature	-70 °C (High sensitivity mode) -75 °C (High Capacity mode)
Dark current @ -75° C operation	0.5 e ⁻ /p/s
Thermoelectric Precision	\pm 0.05 °C over the entire temperature range.
Operating environment	5 to 30 °C non-condensing



Figure 11, PIXIS:400BR Focal plane Array Picture.

The PIXIS: 400BR camera, Figure 11, is designed for low light level spectroscopy or imaging applications. Some of the specifications of the PIXIS: 400BR camera is given in Table 3. The camera operates optimally between 5°C and 30°C. Generally lowering the temperature of the FPA enhances the quality of the acquired signal. PIXIS: 400BR camera has controlling software which controls the temperature and maintains it within ± 0.05 °C of the set temperature by controlling the camera's cooling circuits [27, 28].

Dark charge is the thermally induced buildup of charge in the FPA over time. The statistical noise associated with this charge is known as dark noise. With the light into the camera completely blocked, the FPA will collect a dark charge pattern, dependent on the exposure time and camera temperature. The longer the exposure time and the warmer the camera, the larger and less uniform the background will appear [27].

Controller gain is software selectable and can have three states 1(low), 2(medium) and 3(high). Low gain allows digitization of larger signals, medium is

suitable for mid-level intensity signal whereas high gain allows low level signal measurement [27].

PIXIS: 400BR camera incorporates dual digitization (100 KHz/2MHz), which means that there is a choice of how quickly data will be digitized. The 2 MHz conversion speed is used for the fastest possible data collection and 100 KHz conversion speed is used where the noise performance is the paramount concern [27, 28].

Megapixel resolution and small pixels allow imaging of very fine details, yet the pixels can be easily binned to improve sensitivity. The resolution is greatly increased by employing a 1340 x 400 imaging array. The electronic shuttering provided in this camera eliminates camera vibration and the ability to bin the camera increases light sensitivity thereby increasing the frame rate. The most prominent advantage of this camera system is that it has a 16-bit digitizer that allows the bright and dim signals to be quantified in a single image [27, 28].

The spectral response, Figure 12, shows that the quantum efficiency is maximum, 88%, within the wavelength region of interest, 650nm to 1050nm used for data collection in this study and it never drops below 20%. The PIXIS: 400BR is a back illuminated CCD, allowing the light to be collected through the back surface. The surface of the back illuminated CCD is etched 15-30 μ m thickness in order to collect light through the back surface. As a result of this modification, no light is lost through absorption and reflection giving these CCD's twice the quantum efficiency of their front-illuminated counterpart. However this process makes them semitransparent in the

NIR region, reflections between front and back surfaces causing them to be partial etalon. This unwanted etalon-like behavior creates spectral as well as spatial etaloning in back illuminated CCD's. To minimize etaloning the PIXIS 400BR is made of thicker silicon, roughly double the thickness of a normal back-illuminated CCD contributing to absorption of NIR light minimizing interference with increasing QE.

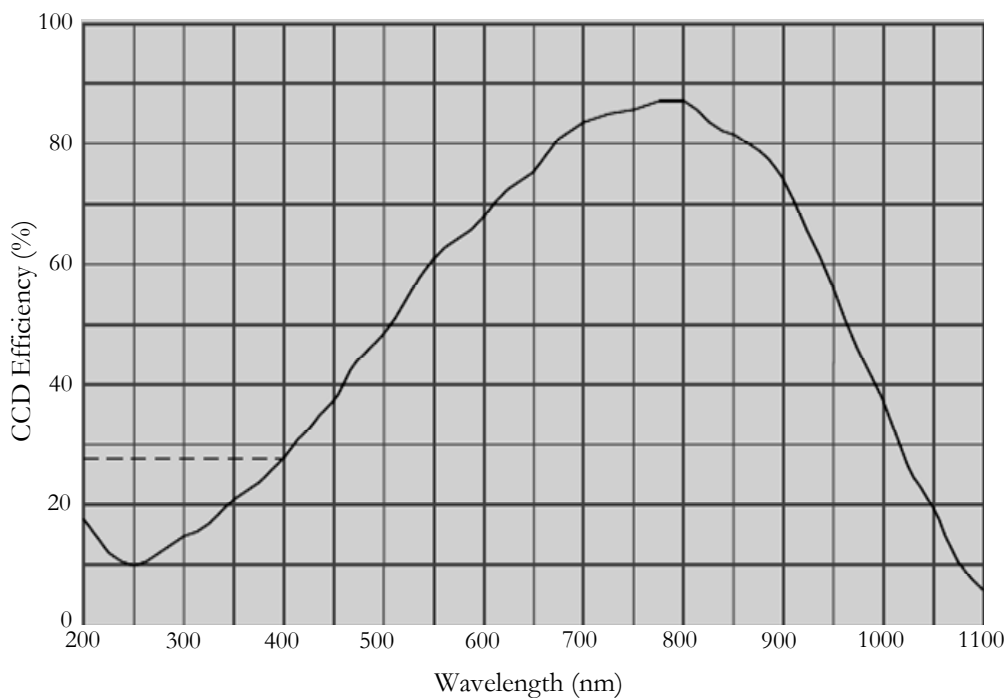


Figure 12, Spectral response for PIXIS: 400BR FPA adopted from Photometrics, Inc.

The AR coating has been optimized for NIR wavelengths, reducing the amount of light reflected into the CCD when the light returns to the CCD back surface from the polysilicon side. The CCD back surface is processed in a proprietary manner that helps to break up the etalon effect [28, 29].

2.1.6.2 CoolSNAP_{ES}

The CoolSNAP_{ES} camera used during the visible region application of the system is a fast digitizing camera manufactured by Roper Scientific (now Princeton Instruments, Inc.). Some of the specifications of the Princeton Instruments CoolSNAP_{ES} camera are given in Table 4.

Table 4, Specification chart for CoolSNAP_{ES} camera.

Specifications	
CCD format	1392 x 1040 imaging array 6.45 x 6.45- μ m pixels 8.77 x 6.6-mm imaging area (optically centered)
Well Capacity	16,000 e- (single pixel) 30,000 e- (2 x 2 binned pixel)
System Read noise	≤ 8 e- rms @ 20 MHz
Nonlinearity	$< 1\%$
Dynamic Range	12 bits @ 20MHz
Frame readout	91 ms/frame
Cooling	Thermoelectric, 5° C below ambient temperature.
Dark current	1 e-/p/s
Operating environment	15 to 30 °C ambient
Dimensions	4.5" x 5.0" x 2.5" (1.9 lbs)

The CoolSNAP_{ES} monochrome camera, Figure 13, incorporates a SONY ICX-285 silicon chip with Interline-transfer capability [30]. Interline-transfer CCD has a parallel register subdivided into alternate columns of sensor and storage areas. The image accumulates in the exposed area of the parallel register and during CCD readout the entire image is shifted under the interline mask into a hidden shift register. Readout then proceeds in normal CCD fashion. Since the signal is transferred in microseconds, smearing is undetectable for typical exposures. However, a drawback to interline-transfer CCDs has been their relatively poor sensitivity to photons since a large portion of each pixel is covered by the opaque mask. As a way to increase a detector's fill factor, high-quality interline-transfer devices have microlenses that direct the light from a larger area down to the photodiode [31].



Figure 13, CoolSNAP_{ES} CCD Image.

Blooming is the migration of electronic charge to the adjacent pixels; however the incorporated Sony chip by Roper Scientific provides protection against blooming by having built in drains that remove any excessive charge generated from an overexposed

pixel. This Sony interline chip will provide anti-blooming for optical signals greater than 1000 times the full well capacity [31].

The electronic shuttering provided in this camera eliminates camera vibration and the ability to bin the camera increases signal to noise ratio while increasing the frame rate. A subcompact, fanless design eliminates the need for a stand-alone power unit [30, 32]. The most prominent advantage of this camera system is the incorporation of a 20 MHz digitizer which provides high speed and high sensitivity readout over a high resolution 1392 x 1040 imaging array [30, 32].

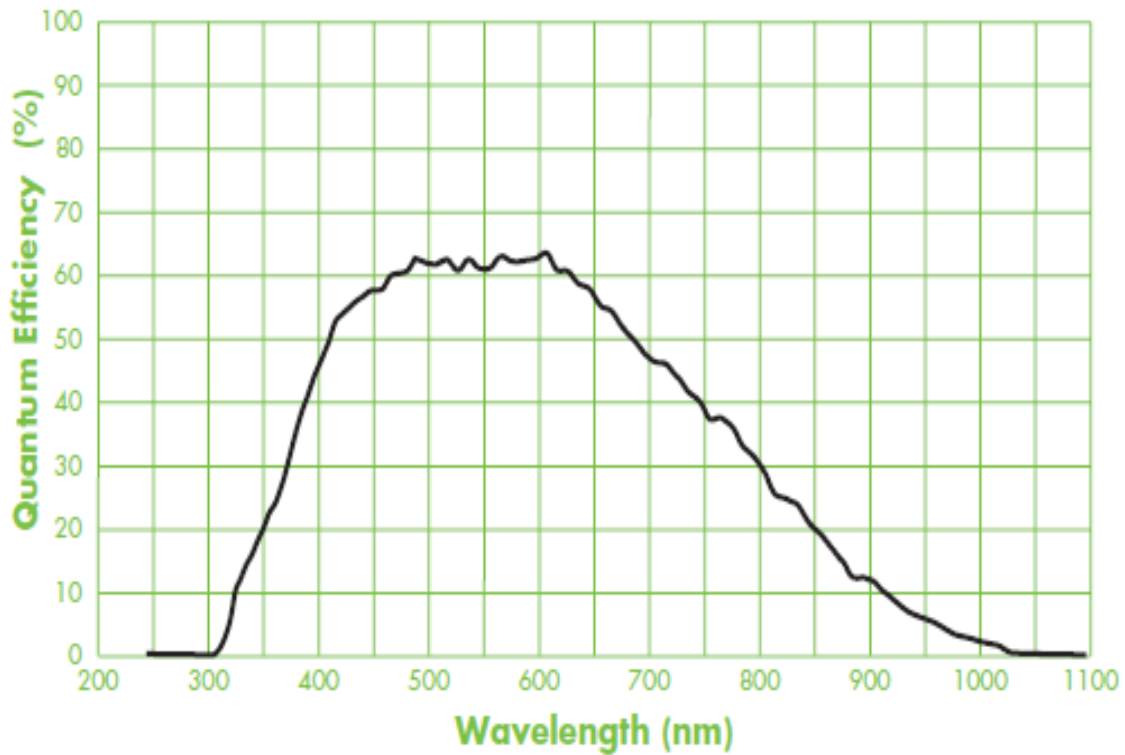


Figure 14, Spectral response of the CoolSNAP_{ES} CCD adopted from Photometrics, Inc.

The spectral response for the CoolSNAP_{ES} camera, Figure 14, within the visible region is the one of interest for the visible system application. The quantum efficiency is always beyond 45% in this region, peaking to over 60% between wavelength regions of 475 to 625 nm.

Both the CCD cameras that is, PIXIS: 400BR and CoolSNAP_{ES} are driven by PVCAM software which stands for Photometrics Virtual Camera Access Method [33]. This software is used to control the cameras and acquire data from them. The data collection process is automated using Vpascal programming language integrated in V++, a precision digital image processing and enhancement software. V++ has been designed to control any PVCAM-compatible feature using the V++ interface and the VPascal built-in programming language [34].

2.1.6.3 Binning

Binning is the practice of merging charge from the adjacent pixels in a CCD prior to digitization in the on-chip circuitry of the CCD by specific control of the serial and parallel registers. Binning reduces the readout time and the burden on computer memory, increases the signal to noise ratio, but at the expense of image resolution. Binning occurs in similar fashions in both PIXIS: 400 BR and the CoolSNAP_{ES} cameras except the latter is an interline transfer CCD whereas the former is a full frame CCD.

To comprehend the binning practice in the Roper scientific cameras, consider the examples shown below in Figure 15, binning 1 x 1 where no charges are summed provides us the maximal resolution against Figure 16, binning 2 x 2 where charges from 4 neighboring pixels are summed. Figure 15(1) shows the CCD at the end of an

exposure, wherein the capital letters represent different charge accumulated on the CCD pixels. Readout of the CCD begins with the parallel readout phase, Figure 15(2), simultaneous shifting of all pixels in a bottom row towards the serial register followed by the serial readout phase, Figure 15(3) and Figure 15(4), shifting of charge in the serial register into the summing well which is then digitized. Only after all the pixels in the bottom row are digitized is the second row from the bottom is moved into the serial register. Thus for example above, the order of shifting is therefore A1, B1, C1, D1, A2, B2, C2, D2, and A3.... and so on.

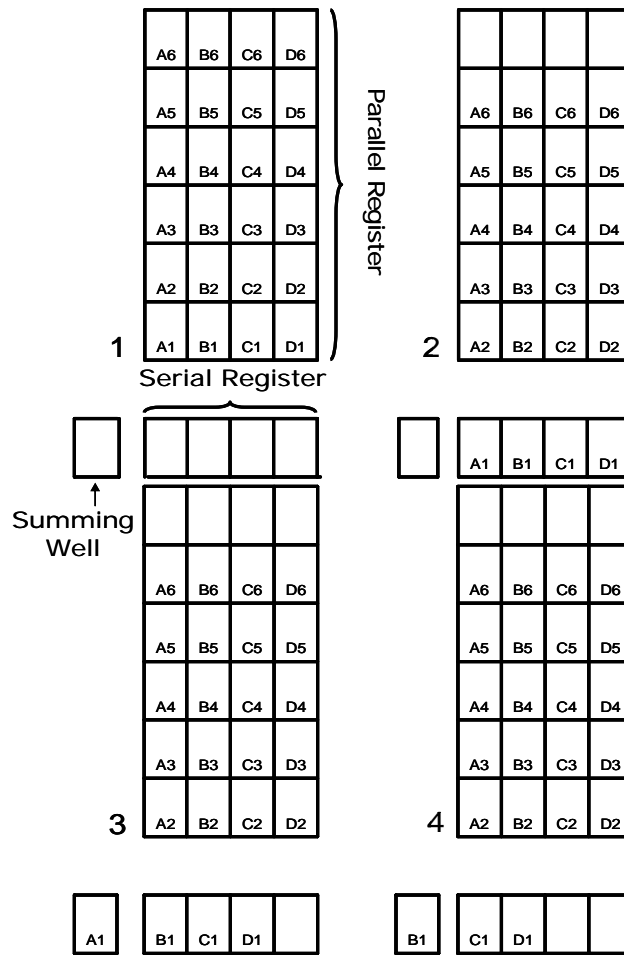


Figure 15, Frame readout, binning 1 x 1.[27]

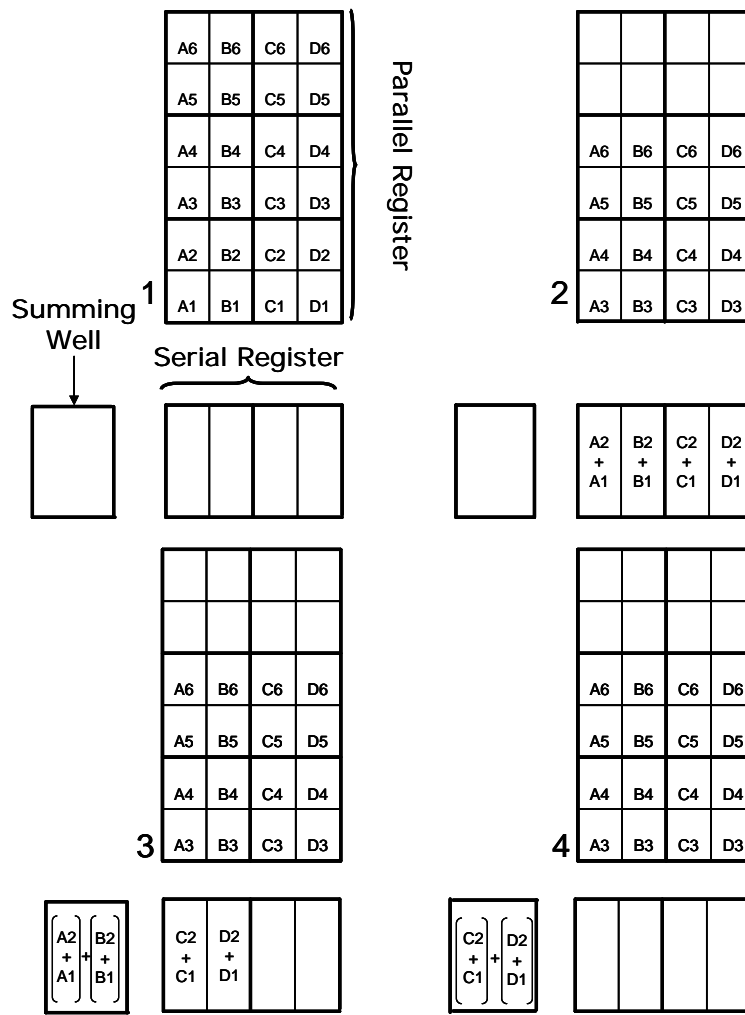


Figure 16, Frame readout, binning 2 x 2. [27]

The charge that has integrated during the exposure is shown as capital letters in Figure 16(1). Readout begins with a parallel readout, Figure 16(2), however, since binning of 2 x 2 is required charge from two rows of pixel, rather than a single row during 1 x 1 binning, is shifted into the serial register. Next, charge is shifted from the

serial register, Figure 16(3) and Figure 16(4), two pixels at a time, into the summing well rather than single pixel as in binning 1 x 1.

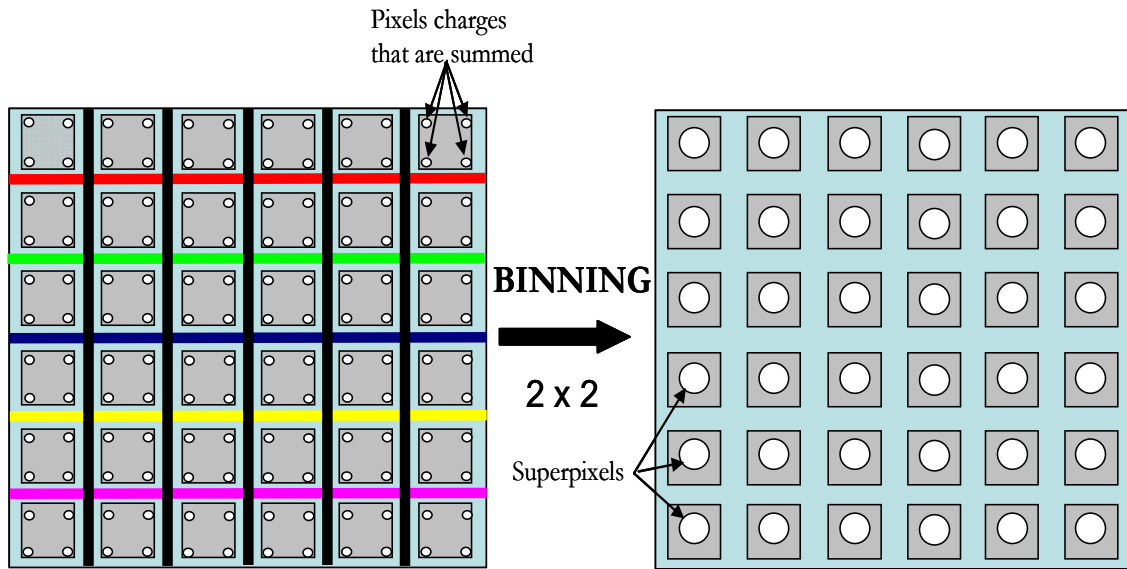


Figure 17, Formation of Superpixels, binning 2 x 2.

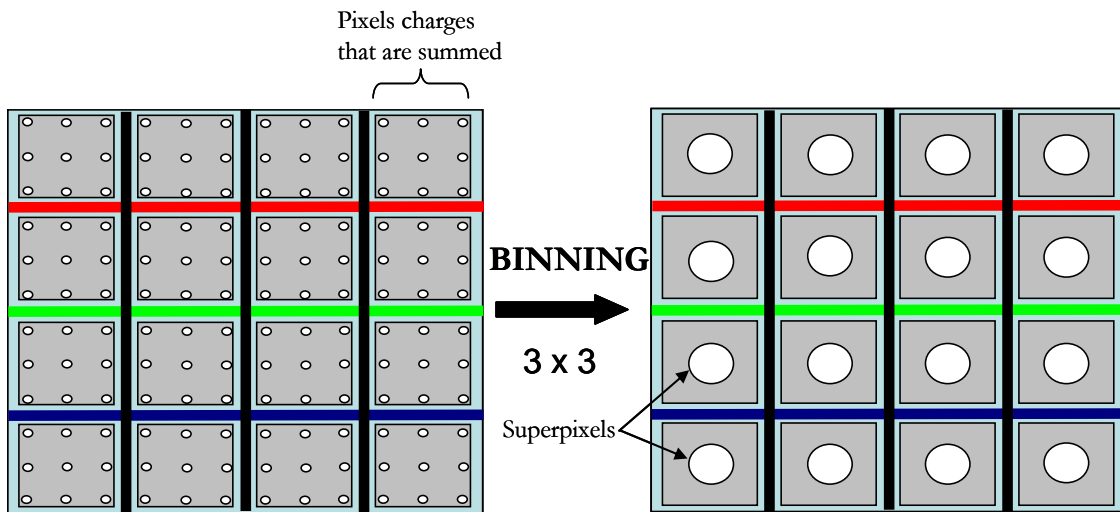


Figure 18, Formation of Superpixels, binning 3 x 3

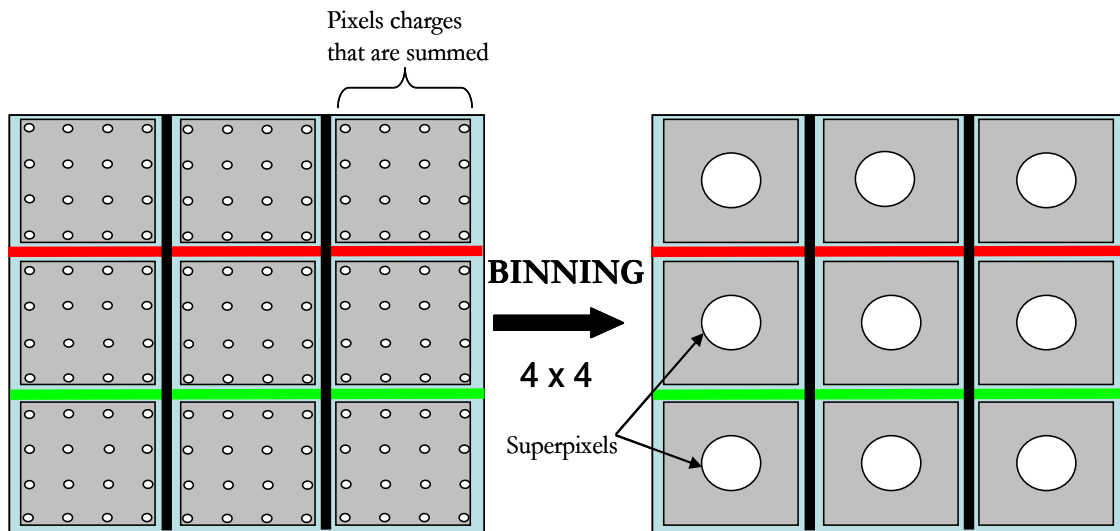


Figure 19, Formation of Superpixels, binning 4 x 4

The result is that each readout event from the summing well contains the collected charge from four pixels on the CCD, superpixel. This procedure is iterated until the entire array has been read and the formation of superpixels shown below for binning of 2 x 2, Figure 17. Similarly superpixel formation for 3 x 3 binning, Figure 18, and 4 x 4 binning, Figure 19 is also shown.

2.2 Experimental Section

2.2.1 Reference Spectra

Hyperspectral data analysis provides spatially distributed contributions of oxyhemoglobin, which is obtained based upon oxy- and deoxyhemoglobin reference spectrums. Pure HbO₂ and Hb solutions were prepared at NIH by standard methods using blood collected from a healthy individual and reference spectra were obtained from the original imaging system developed at NIH for the Visible region (400-700

nm). A region of interest (520-645 nm) containing the peaks for oxy- and deoxyhemoglobin was selected and used for imaging purposes in the visible region, Figure 20.

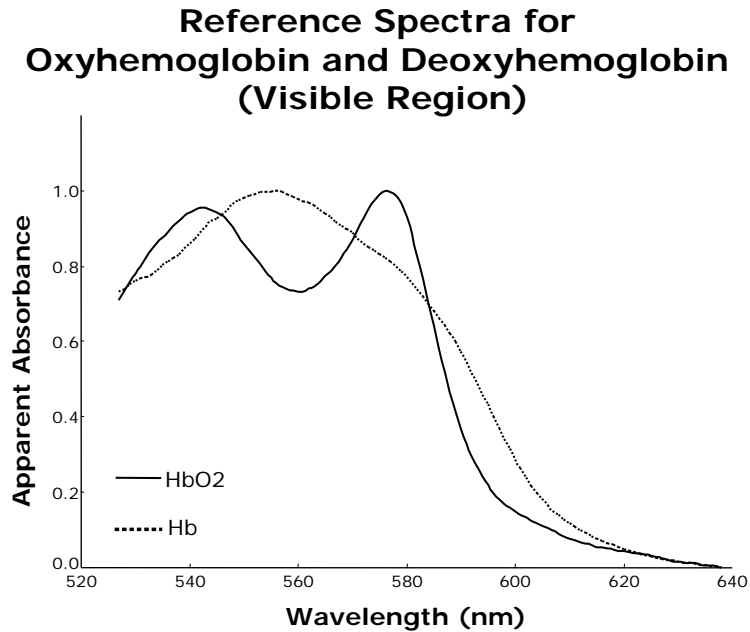


Figure 20, Reference spectra for Oxyhemoglobin and Deoxyhemoglobin within Visible region. [3]

Similarly a region of interest (650 –1050 nm) in the Near Infrared light spectrum which extends between 700-2500nm was selected for detecting contributions of oxyhemoglobin in the hyperspectral images using the reference spectra, Figure 21 [35, 36].

Reference Spectra for Oxyhemoglobin and Deoxyhemoglobin (Near Infrared Region)

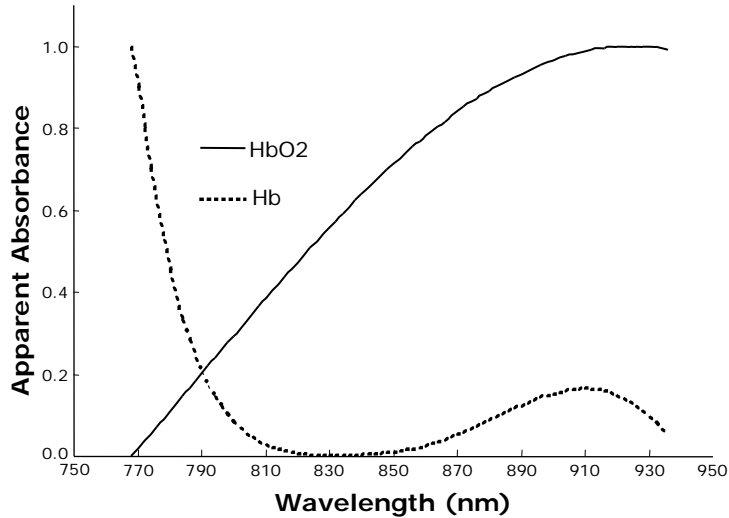


Figure 21, Reference spectra for Oxyhemoglobin and Deoxyhemoglobin within the Near Infrared region. [37]

2.2.2 Experiment Protocol

A proof of principle clinical study involving the dermal microvasculature of ten subjects was performed to demonstrate the functioning of the system as a tool to measure contributions of oxyhemoglobin. The data collection during this clinical study was done at the Laboratory of Biomedical Imaging, UTA, under the supervision of Dr. Karel Zuzak, Ph.D., after receiving approval from The UTA Institutional Review Board, IRB.

The subjects briskly strolled for 15 minutes preceding data collection after which they entered the lab. Upon entering the lab normal room light were turned off and the skin tissue of interest, within the palm of the hand was marked using a standard

office marker where the mark served as a spatial reference to control/ensure the spatial location of the tissue being imaged stayed the same. The palm was chosen instead of the forearm, leg, or posterior of the hand because of its relatively low melanin content. This reduced amount of melanin, the pigment responsible for skin tone, minimizes the effect that skin pigmentation may have on the measured reflectance spectra [38].

A second study involving seven subjects, was undertaken under supervision of Dr. Karel Zuzak, at UTA, for imaging the Human eye after seeking approval from the Institutional Review Board, IRB. In this study, the sclera of the eye was illuminated using the light source from the slit lamp for 5 seconds while acquiring a the Hyperspectral image cube. The imaging was achieved in two steps, firstly on entering the lab, the subjects were asked to rest their chin on the chin rest of the slit lamp with closed eyes and light from the slit lamp was shone onto one of the closed eyelid which was brought in focus of the slit lamp. Secondly, upon getting the eyelid in focus using the slit lamp optics, the subjects were then asked to open their eyes, look in the opposite direction from where the light was shone into the eye, and the slit lamp was made to focus on the scleral vessels upon which, hyperspectral image data cube was obtained for 5 seconds.

2.2.3 Data Acquisition

The experimental setup for our noninvasive microscopic reflectance hyperspectral imaging system consisting of a source, optics, filter and detector is illustrated in Figure 16. The Slit lamp contains a 12V/30W halogen source providing broad band

illumination, that illuminates the target and the reflected light from the target is guided by the microscopic optics onto a beam splitter, a semi-silvered mirror transmitting light to the eyepiece and to the attached hyperspectral imaging system. The radiation from the beam splitter is directed towards the LCTF using relay optics. The LCTF differentiates the broadband reflected light provided by the source into individual band

Microscopic Hyperspectral System

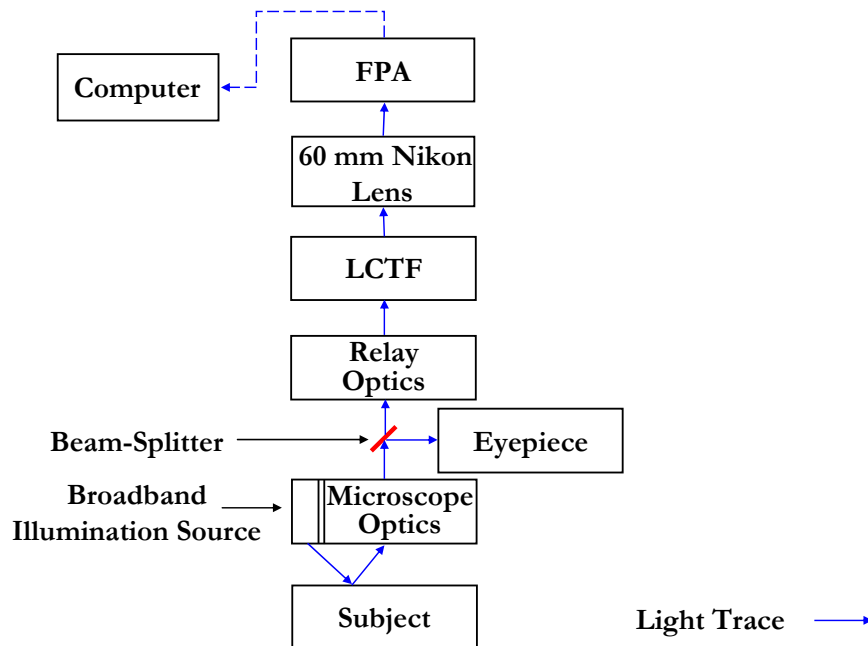


Figure 22, Experimental setup for the Clinical Study.

passes of wavelengths that are placed on the focal plane array (FPA) detector with the use of a 60 mm Nikon lens fitted in front of the FPA. The FPA has an analog to digital, A/D, converter for digitizing the data, which is transferred it to a high end laptop PC for post processing. A computer program automatically manages the data collection by synchronizing the timing between individual hardware components, for example, tuning

the LCTF and triggering the FPA, and setting experimental parameters (image size, exposure time, spectral range and resolution, image binning, gain, filename) using a GUI that was built in V++. To sum up the data acquisition, various experimental parameters are inputted initially using the GUI developed in V++, after which the LCTF initializes and the desired voltages calculated for the spectral range selected are stored into the palette. Upon initialization, the LCTF tunes to the first wavelength specified in the palette, the camera is triggered, the CCD is exposed for the duration of the exposure time, and ADC digitizes the image information storing it onto the Laptop. This process is repeated for the remaining wavelengths.

For the near infrared application, the focal plane array (FPA) used was the PIXIS: 400BR in combination with the NIR LCTF. The raw hyperspectral image data was collected over a spectral range of 650–1050 nm with a spectral resolution of 5 nm increment with the magnification set at 10X and CCD binning of 1 x 1 for maximizing image resolution. The exposure time of the CCD set for each image was 17 ms, resulting in an entire reflectance hyperspectral image cube being acquired and saved to hard disk in around 35 seconds.

For the visible application, the focal plane array (FPA) used was the CoolSNAP_{ES} CCD in combination with the visible low resolution LCTF. The raw hyperspectral image data was collected over a spectral range of 520–602 nm with a spectral resolution of 2 nm increments with the magnification set at 10X and CCD binning of 2 x 2 for increasing readout speed. Thus an entire reflectance hyperspectral image cube was acquired and saved to hard disk in around 5 seconds.

2.2.4 Determination of Experimental parameters

For the near infrared application the wavelength range 650 – 1050 nm is selected since the PIXIS: 400BR quantum efficiency falls below 10% beyond 1050nm yielding noisy data. Also within this range deoxy- and oxyhemoglobin have distinct spectra which can be used to obtain contributions of oxyhemoglobin. The LCTF contains a palette formed of 128 distinct registers that store voltages for the associated desired wavelengths that are determined prior to acquisition and stored in the palette. If more than 128 wavelengths are desired, the palette initially holds the voltage values for the initial 128 wavelengths, and it re-initializes during acquisition to calculate values for the remaining wavelengths, increasing the exposure time per hyperspectral image cube. Since, one of the goals is to keep the acquisition time for the data cube at its lowest, wavelength range is so selected that the total desired wavelengths stay below 128. Hence for the near infrared system the wavelength range 650 – 1050 nm is selected with a spectral resolution of 5 nm giving us a total of 81 wavelengths.

Further, magnification of the system which is determined by the slit lamp optics is interchangeable between 10X, 16X and 25X. An experiment was performed using the visible microscopic hyperspectral imaging system wherein a ruler was placed in field of view and imaged for magnification of 10X, 16X and 25X. These images were analyzed using matlab to find number of pixels in between 1 mm scale lines in each image yielding 49 pixels per mm with magnification 10X, whereas 79 pixels within magnification 16X and 131 pixels within magnification 25X. Thus as the magnification

increases, the same 1 mm region occupies more number of pixels indicating more number of resolvable points per mm which is nothing but the spatial resolving power of the system under different magnification. However, this increasing spatial resolution comes at the cost of reduction in the field of view. Also the depth of field is reduced with increase magnification. The image brightness decreases with increased magnification requiring a higher exposure time as demonstrated above increasing the overall exposure time, for example this particular ruler experiment requires 2ms of exposure time for 10X magnification while 16X requires 12ms and 25X requires 35ms of exposure time. Hence, increasing the magnification will increase the image resolution and the ability to visualize smaller blood vessels reducing the field of view and the image brightness thus increasing the total acquisition time. This made us collect data at magnification 10X, the lowest of the magnification that can be achieved by the slit lamp.

The transmittance of the system is dependent on the spectral output from the slit lamp optics, the relay optics, the LCTF, the Lens and the FPA. Thus to obtain the spectral output of the entire system experimentally, a 99% reflectance surface, Spectralon, is placed in the light path and hyperspectral image cube is obtained within the spectral range 650 -1050 nm , binning of 1 x 1 and the spectral resolution of 5 nm. Figure 23, determines the spectral output of the system after analyzing the hyperspectral image data cube which shows us that the transmittance of the system is wavelength dependent peaking at 750 nm in the near infrared region for the specific LCTF and the FPA used in the system.

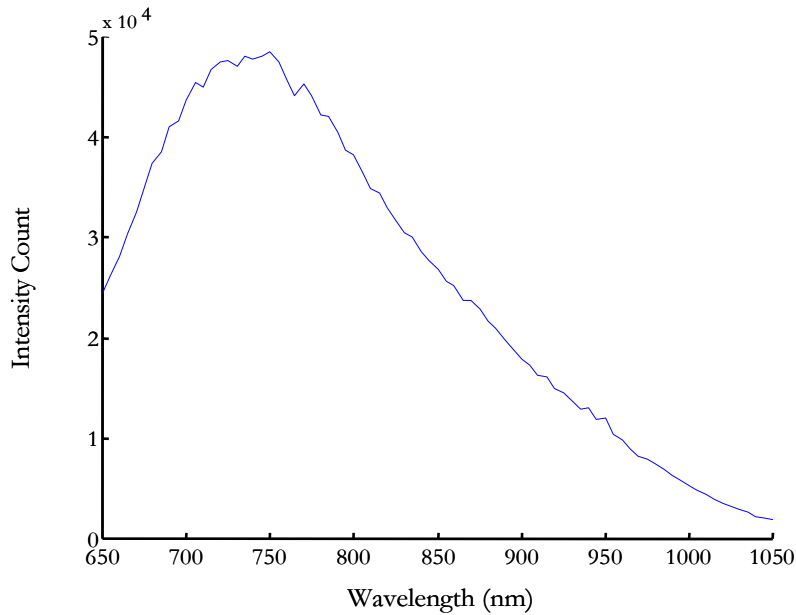


Figure 23, Output spectrum for the Near infrared microscopic hyperspectral system.

The exposure time for the microscopic near infrared hyperspectral system is obtained experimentally by tuning the LCTF 750 nm, highest transmittance of the system, and placing the spectralon surface in the light path while the reflected light from the spectralon surface was captured by the camera being displayed in image format by the V++ software along with the maximum light intensity count in the image. The magnification of the system was set at 10X and the camera lens aperture was set to the smallest F-stop to allow maximal light onto the FPA. The FPA contains a 16 bit A/D converter; hence the maximum count reached by the FPA pixels is 65535 counts. But as a safety buffer, the exposure time, 17ms for near infrared system, is obtained when the maximum pixel count in the image reaches 60000 counts instead of its full range which is 65535 counts.

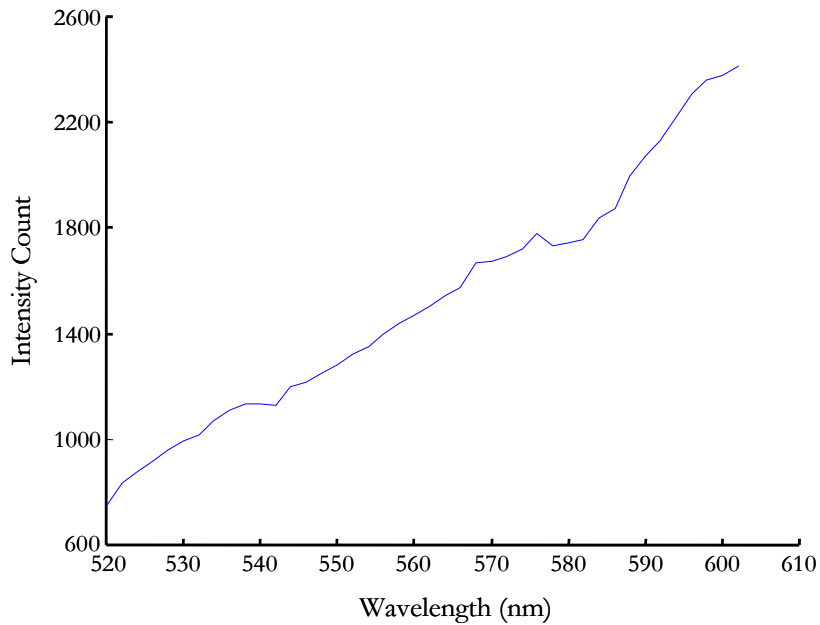


Figure 24, Output spectrum for the Visible microscopic hyperspectral system.

The microscopic hyperspectral system was also used to image the anterior region of the human eye making it pertinent to reduce the acquisition time for the entire hyperspectral cube well below 35 seconds. Hence, the PIXIS: 400BR having a 2 MHz digitizer was replaced with the CoolSNAP_{ES} FPA that utilizes a 20MHz digitizer thus increasing the frame readout cutting the exposure time nearly in half over the PIXIS FPA. Further, the raw hyperspectral image data was collected over a spectral range of 520–602 nm, using a visible region LCTF instead of NIR LCTF, with a spectral resolution of 2 nm increments. Previous macroscopic studies in visible hyperspectral imaging have used the visible region 520-645nm over which oxy- and deoxyhemoglobin have distinct spectrum giving us 126 wavelengths at 1 nm resolution. But, in the interest of reducing the exposure time, the wavelength range of 520 – 602 nm was selected with a spectral resolution of 2 nm giving us 42 wavelengths. The

magnification was set at 10X and CCD binning of 2 x 2 though helped increase the frame readout, reducing image acquisition time at the cost of image resolution, since binning limits spatial resolution of the system. These all factors allowed limiting the total acquisition time for the entire hyperspectral cube to 5 seconds, which is very suitable for any imaging application of the eye. The exposure time for the system after setting up all these parameters was calculated experimentally as detailed above by setting the LCTF to the highest transmittance wavelength, 645 nm depending on the spectral output, Figure 24, and putting the spectralon surface in the light path imaging it onto the CoolSNAP_{ES} FPA via the V++ software. The CoolSNAP_{ES} FPA has a 12 bit digitizer hence 4095 is the maximum counts the pixel can hold thus keeping a safety buffer the exposure time was selected when the camera reached a maximum intensity count of 3500 counts.

2.2.5 Data Analysis

Matlab (Mathworks, Natick, MA) was used for writing hyperspectral image processing and analysis programs developed in our laboratory. Images of relative contribution of oxyhemoglobin are generated from the measured spectrum, which is assumed to be a convolution of oxyhemoglobin and deoxyhemoglobin reflectance spectra. Measured Image reflectance spectra are first transformed to apparent absorption units, the data is smoothed by a Savitzky-Golay polynomial filtering method and then normalized to the maximum spectral peak at each pixel.

The raw hyperspectral images of the subject are converted to apparent absorbance units (A_{xy} , Equation 1) by ratioing against the raw hyperspectral images of

a 99% reflectance standard, Spectralon, (Lab-sphere Inc., SRT-99-120, Sutton, NH), which provides the $R_{xy}(l)_{standard}$ term in the apparent absorbance equation by the measured reflection incident from the sample, $R_{xy}(l)_{sample}$, at wavelengths, l , for the spatial position x & y [39-42].

$$A_{xy}(\lambda) = \log_{10} \left(\frac{R_{xy}(\lambda)_{standard}}{R_{xy}(\lambda)_{sample}} \right).$$

Equation 1, Apparent Absorbance Units Conversion.

The Savitzky-Golay method, equation 2, filters the data by implementing a moving window approach reducing the useful spectral range to 685 – 1015 nm in the near infrared region application and to 534 – 588 nm for the visible region application [43].

$$g_i = \sum_{n=-nL}^{nR} c_n f_{i+n}$$

Equation 2, Savitzky-Golay filter equation. [43]

where, $C_n = \{ (A^T \cdot A)^{-1} \cdot (A^T \cdot f_n) \}$

$A_{ij} = i^j, j = 0, \dots, M; M = \text{polynomial order.}$

Equation 3, Savitzky-Golay filter equation definitions. [43]

The filter is applied to a series of equally spaced data value f_i , which is replaced by a linear combination g_i , the average of the data points from f_{i-nL} to f_{i+nR} . The idea of the savitzky golay filtering is to find filter coefficients c_n for each point f_i , least square

fitting a polynomial to all points n_L+n_R+1 in the moving window and then set g_i to be the value of that polynomial at position i . In our case f_i is either the data value, where i , represents wavelengths for apparent absorbance values at each wavelength while obtaining spectroscopic information or f_i is the pixel value where i , reflects the pixel location with respect to a select location ($i = 0$) on the image data in the hyperspectral data cube while obtaining quantitative values.

The measured spectrum is then deconvoluted by performing a least-squares fit for each detector pixel to determine the best linear combination of the oxy- and deoxy-hemoglobin reference spectra

CHAPTER 3

RESULTS

3.1 System Characterization

The Microscopic Hyperspectral Imaging System developed at UTA was characterized. The characterization of the system involved the characterizing the LCTF, the FPA and the slit lamp source. The LCTF was characterized for its Spectral band-pass, Tune Delay, and the Tuning wavelength capability of the filter. The FPA was characterized for its ability to differentiate between objects, spatial resolution. The Slit lamp source was characterized for its Intensity and temperature.

3.1.1 Slit Lamp Source

The Slit lamp source is a 12/30W halogen lamp that provides the source of illumination for the imaging applications. It was calibrated for the light intensity it produced at different varying distances. Light intensity is an indication of the strength of a light source and it decreases with increasing distance. The slit lamp source can be considered as a point source that emits light of a given power spreading evenly in all direction. As the distance of illumination increase from the source more is the surface area illuminated. The surface area can be considered to be a sphere in this case and is

proportional to the square of the radius. Thus the light intensity which gets distributed evenly over this surface area falls off as a square of the distance [44]. A NIST standard calibrated light meter (Cal-Light 400, Cooke Corporation, MI) with a silicon photodiode sensor, providing direct measurement within 0.1 – 40,000 lux or footcandle units was used [45]. Light intensity was measured at every inch using the light meter increasing the distance up to 51 cm which is plotted in the Figure below.

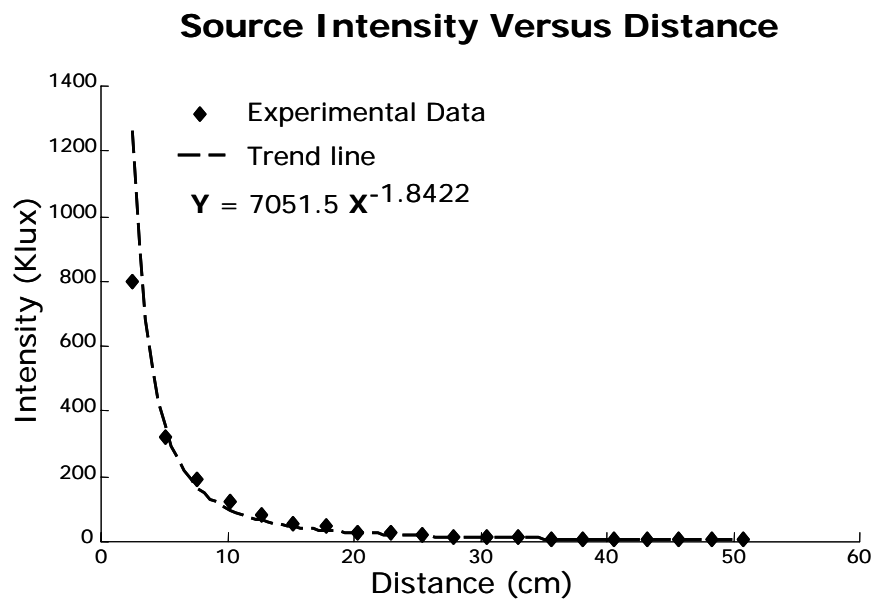


Figure 25, Slit Lamp Source Intensity Versus Distance.

The experimental data plotted above allows us to get a relationship between the Light intensity and the distance from the source which is the equation displayed in the plot where ‘y’ displays the intensity and ‘x’ represents the distance from the source, Figure 25. For the imaging application the target is placed at a distance of 10 cm from the source thus being illuminated with a light intensity of approximately 100 Klux.

Further, the slit lamp is a broadband source, i.e. it includes the Visible as well as Near Infrared light. Near infrared light is a source of heat and could potentially lead up to severe burn injuries in the subjects. Thus temperature readings of the lamp source, keeping the same experimental setup used during subject data collection are measure and plotted, Figure 26. Briefly, the temperatures were measured by placing a calibrated digital thermometer in the light path at the same distance as the source target.

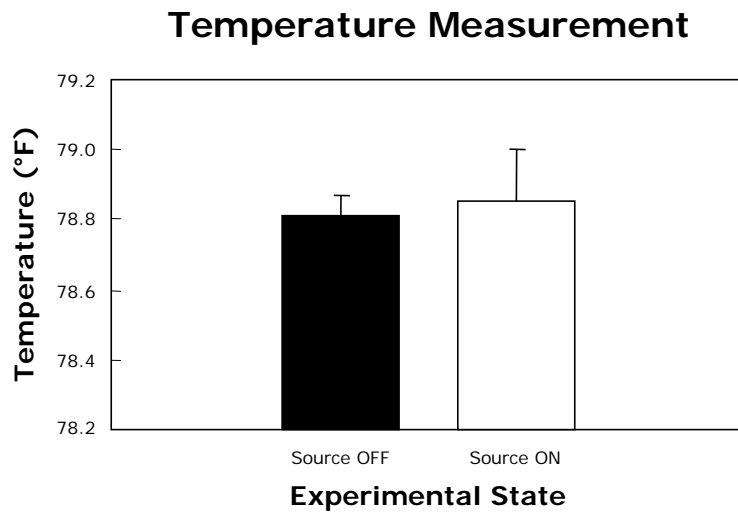


Figure 26, Comparison of average temperature variations over a period of 30 seconds with the Source Off and Source On.

Firstly, a temperature reading was taken when the source is OFF, i.e. the ambient temperature of the room, followed by turning the source ON and recording the temperature reading after a period of 30 seconds, the maximal experimental time period for collecting one hyperspectral cube between the dermal tissue experiment and the Human eye imaging experiment. This procedure was repeated ten times providing a mean temperature reading, Figure 18, for the slit lamp source. Comparing the sampled temperature measures with source On versus source Off, using a standard T-test, we

obtain a P values of 0.167 (two-tail) which is greater than 0.05, level of significance, indicating that the source does not increase the temperature during subject data collection conditions for either of the experiments.

3.1.2 LCTF Calibration

The spectral capabilities of the near infrared LCTF were determined using a calibrated Perkin Elmer Spectrometer (Perkin Elmer, U.S.A) from Dr. Hanli Liu's laboratory at UTA. The spectrometer was scanned in increments of 1 nm with the near infrared LCTF that was tuned to a specific wavelength placed in the collimated optical path of the spectrometer. This procedure was repeated for a series of sequential wavelengths spanning the range of the near infrared LCTF, 650 nm to 1000 nm, at every 50 nm and the corresponding transmittance spectra of the LCTF were noted. The transmission spectra from the spectrometer were then analyzed in Matlab to measure the center wavelength the LCTF actually tuned to.

The desired wavelengths that were electronically sent to the LCTF controller are plotted on the X axis and the measured wavelengths, the spectrometer transmission spectral analysis, to which the LCTF tuned, are plotted on the Y axis, Figure 27. Points in the Figure 27 are experimental values and the dashed line represents a linear regression curve fit ($Y = 1.00 X - 0.20$, $R^2 = 1$). From the experimental data we appreciate the fact that an error exist between the desired tuning and the actual tuning of the LCTF. To rectify this small error we setup a look-up table in the V++ software from

the relationship that we derive above which makes sure that the LCTF gets tuned to the wavelength which the operator desires

Near Infrared LCTF Calibration

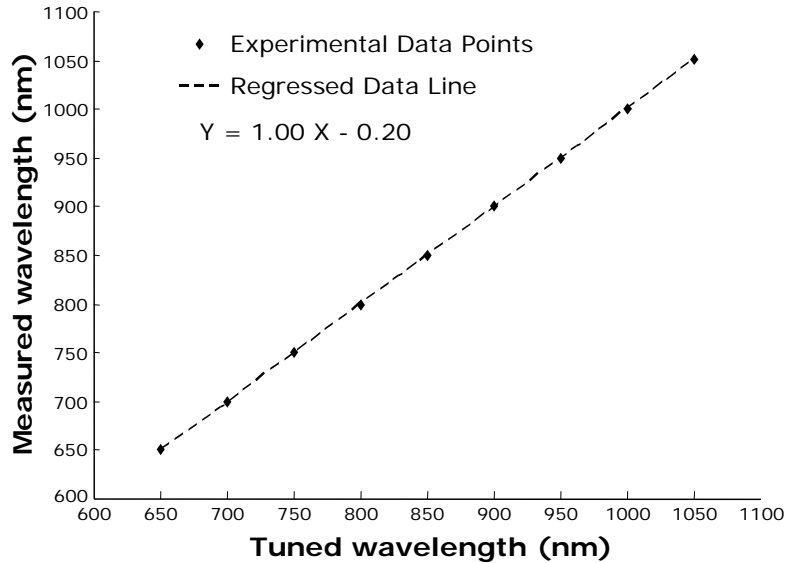


Figure 27, Near Infrared LCTF calibration curve with the dash line indicating the regressed line.

The visible low resolution LCTF similarly was calibrated, however, we used a high resolution LCTF, Band-pass lying between 0.19 at 500nm and 0.75 at 700nm, calibrated here at UTA as the spectrometer in the experiment [46]. As you can see from the experimental setup, Figure 28, the input light from the source is passed through the Low resolution LCTF, which is to be calibrated, tuned to a particular wavelength onto the high resolution LCTF which is scanned with an increment of 1nm over its spectral range of 480-720 nm and focused using the 60mm Nikon camera lens onto the CCD

camera generating a series of images, hyperspectral image cube. This procedure was repeated until we tune the low resolution LCTF in the wavelength range 500-700 at

VISIBLE LOW RESOLUTION LCTF CALIBRATION SETUP

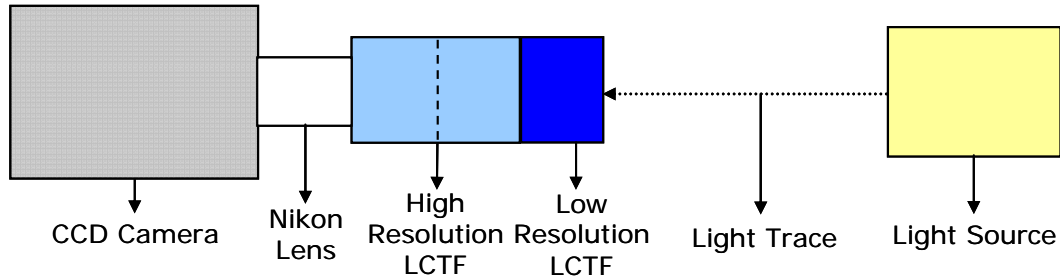


Figure 28, Visible Low resolution LCTF calibration curve experimental setup.

every 10nm and capture hyperspectral cube. The hyperspectral cubes generated were then analyzed in Matlab to locate the center wavelength the LCTF actually tuned to.

Visible Low Resolution LCTF Calibration Curve

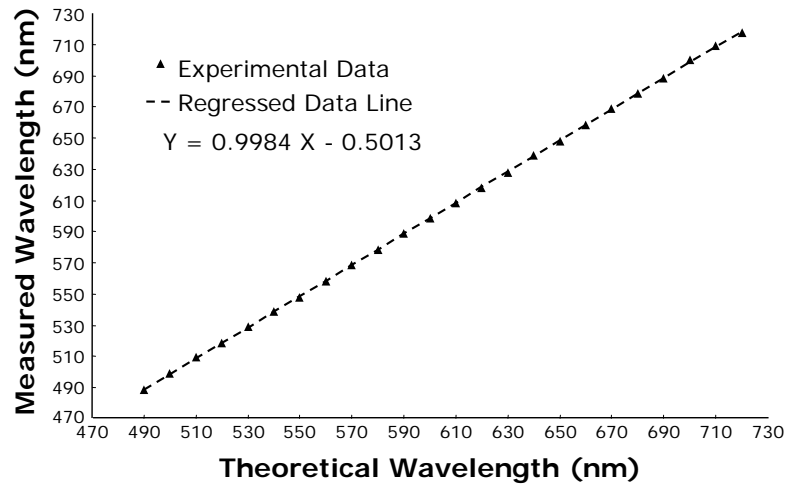


Figure 29, Visible low resolution LCTF Calibration curve.

As in the near infrared LCTF calibration plot, here also the desired wavelengths sent to the LCTF controller are plotted on the X axis and the measured wavelengths from the hyperspectral analysis are plotted on the Y axis, Figure 29. Points in the Figure 29 are experimental values and the dashed line represents a linear regression curve fit ($Y = 0.9984 X - 0.5013$, $R^2 = 0.9999$). From this relationship, we generate a small look-up table in the V++ software tuning the LCTF to the desired wavelength that the operator desires.

Bandpass (NIR LCTF : 50970)

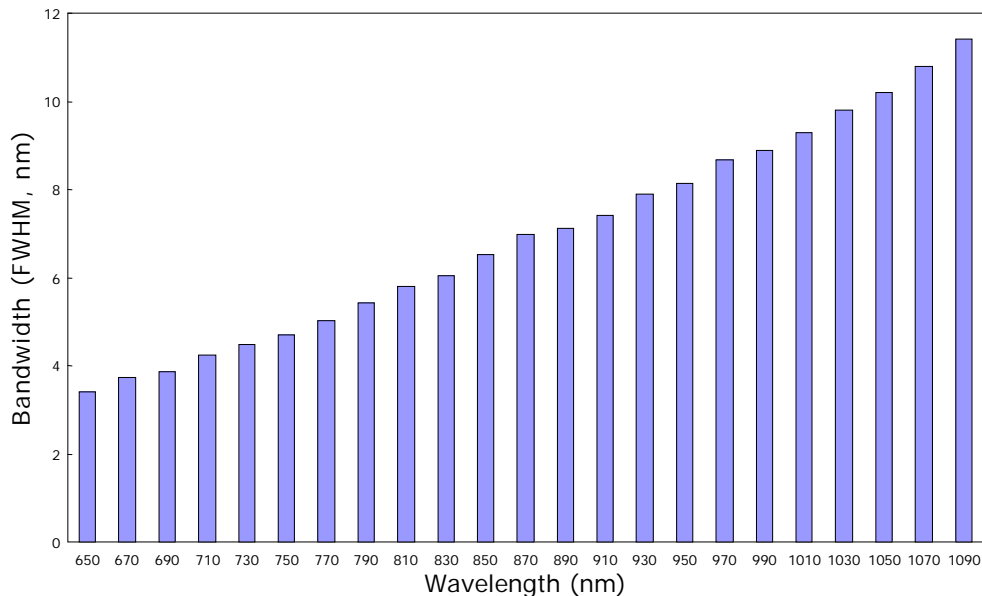


Figure 30, Spectral Band-pass plot for Near Infrared LCTF.

The NIR LCTF spectral band-pass linearly varies at the function of the wavelength, 3.4nm at 650 nm to 11.4 at 1090nm, Figure 22. Similarly the spectral band-pass for the visible low resolution filter varies from 3.7nm at 400nm to 12.2 nm at

700nm, Figure 30. The conclusion from these Figures is that the LCTF band-pass is wavelength dependent. This bandwidth is more than sufficient to spectroscopically resolve HbO₂ and Hb which have spectral characteristics that are several times broader than the broadest band-pass.

Bandpass (Visible LCTF : 51005)

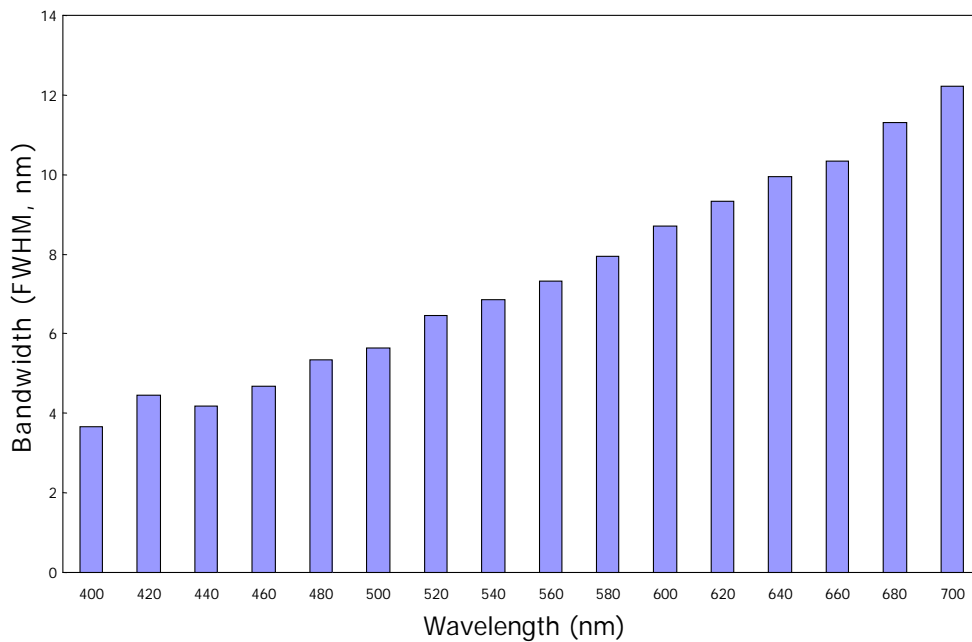


Figure 31, Spectral Band-pass plot for visible low resolution LCTF.

In the hyperspectral imaging system images are collected sequentially at wavelength differentiated continuously by the LCTF that tunes from one wavelength to another. LCTF takes typically 50 to 150ms to switch from one wavelength to another, the response time [25]. Any imaging application collecting sequential image data through the LCTF must account for the response time required by the tune the LCTF. In

the V++ program developed to control the acquisition of the hyperspectral imaging system a tune-delay time is introduced that accounts for the LCTF tune time

TUNEWAIT EXPERIMENT SETUP

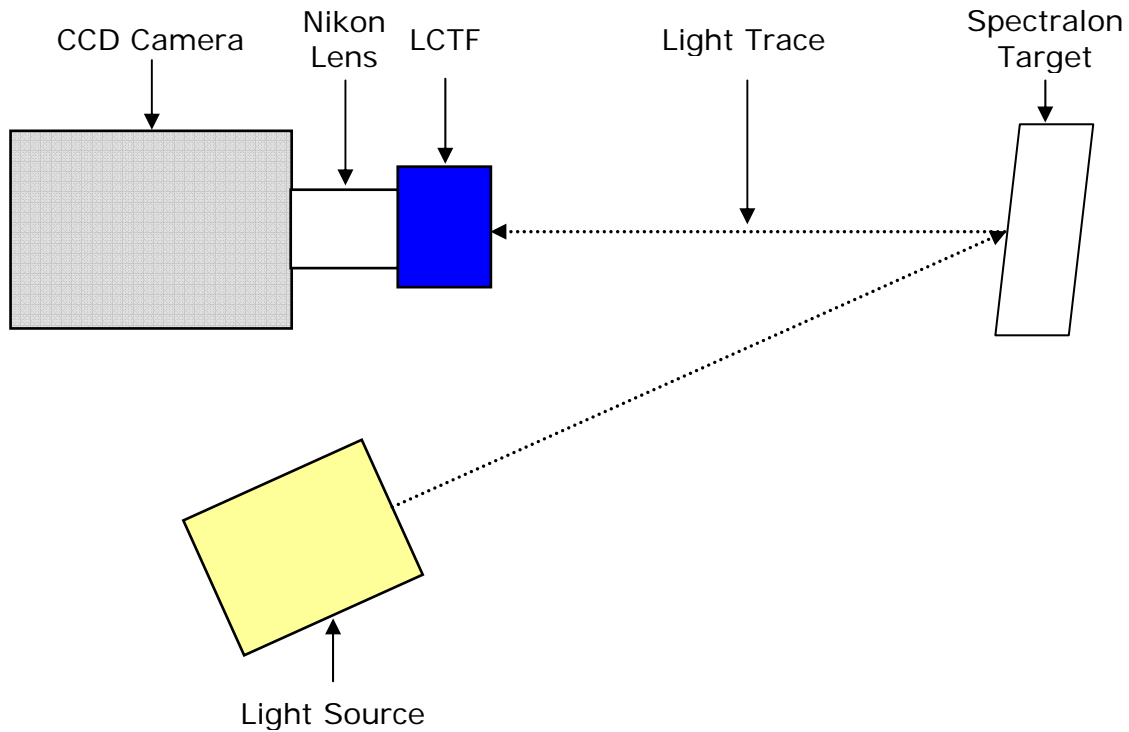


Figure 32, Tune Delay/Tunewait time experimental setup.

An experiment was performed to determine this tune-delay or tunewait time for the LCTF's; the setup for which is shown in the Figure 32. In this experiment light focused on a spectralon target is reflected onto the FPA through the LCTF and a hyperspectral cube was collected. Hyperspectral cubes were collected for varying tune-delay time starting from 0ms until 100ms in increment of 10ms.

NIR LCTF TUNEWAIT EXPERIMENT

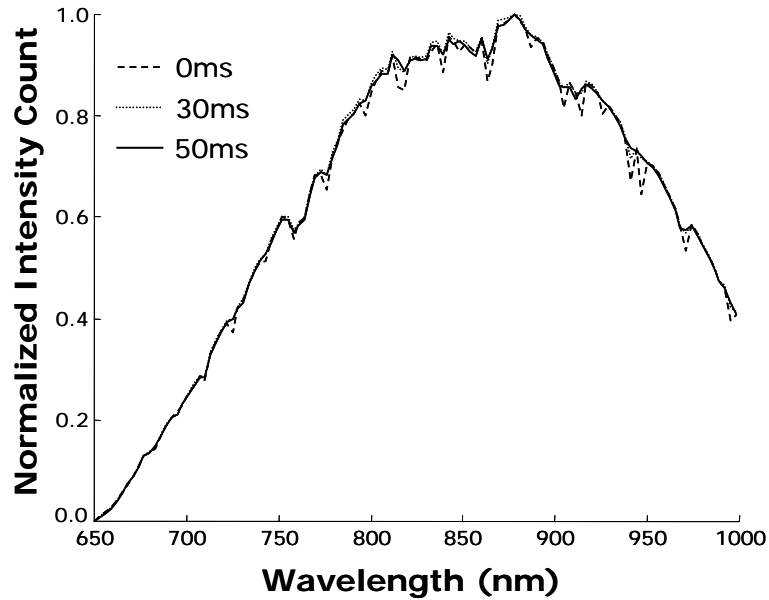


Figure 33, NIR LCTF Tune Delay time experimental outcome.

Figure 33 shows spectral analysis of the hyperspectral cubes collected in the near infrared region using the PIXIS:400BR FPA and the NIR LCTF. The spectrum at tune-delay time of 0ms, dashed line, shows spikes which begin to disappear as tune-delay time is increased, hence tune delay time of 50ms typically should be considered while acquisitioning data using the NIR LCTF. Similar, spectral analysis was performed on the Visible LCTF and from the Figure 34 below there is little or no difference between 0ms, 30ms and 50ms, thus suggesting a tune-delay of 0ms for the Visible LCTF.

The tune-delay time increases the exposure time for collecting the hyperspectral hence keeping it to the minimum is advantageous. Tunewait/Tune-delay time depends

on various factors such as the liquid crystals, the electronic components in the circuitry hence tunewait time is typical for each LCTF [20, 25].

VISIBLE LCTF TUNEWAIT EXPERIMENT

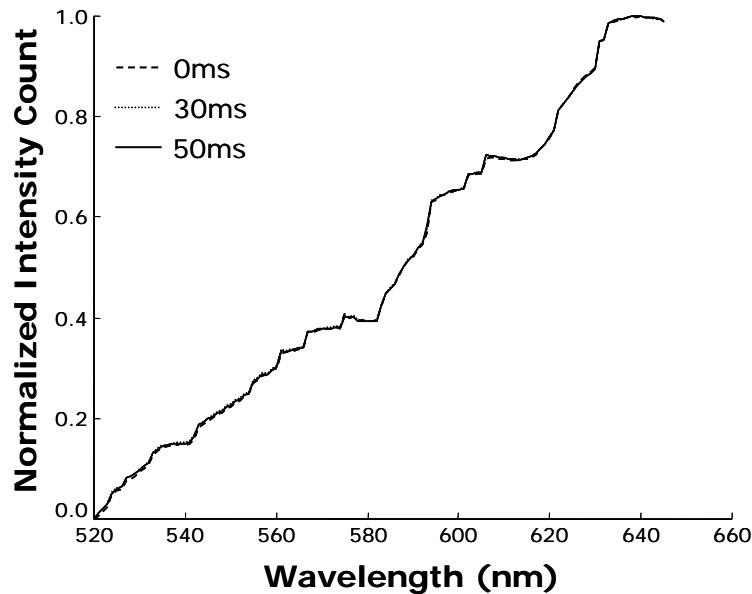


Figure 34, Visible LCTF Tune delay time experimental result.

3.1.3 FPA Calibration

The Spatial resolution of the microscopic hyperspectral imaging system was characterized, which is defined as the ability to distinguish between two closely spaced objects on an image. The spatial resolution of the system was established by computing the percent contrast which depends on various factors such as Focal plane array, filter, slit lamp magnification, type of camera lens, f -stop, depth of field, and degree of pixel binning. Modifications of any of the factors alter the spatial resolution of the system,

thus spatial resolution was evaluated with various degree of binning and magnification. The Percent Contrast, C , was experimentally determined from the expression equation (3), and plotted as a function of spatial resolution in millimeter.

$$C = \left(\frac{I_{\max} - I_{\min}}{I_{\max} + I_{\min}} \right) \times 100$$

Equation 4, Percent contrast Determination.

where I_{\max} , maximum intensity reflected by a line of the resolution target (white bar) and I_{\min} , minimum intensity from the nonreflecting area between the lines (dark bar) of the resolution target [38] are shown in Figure 35 below.

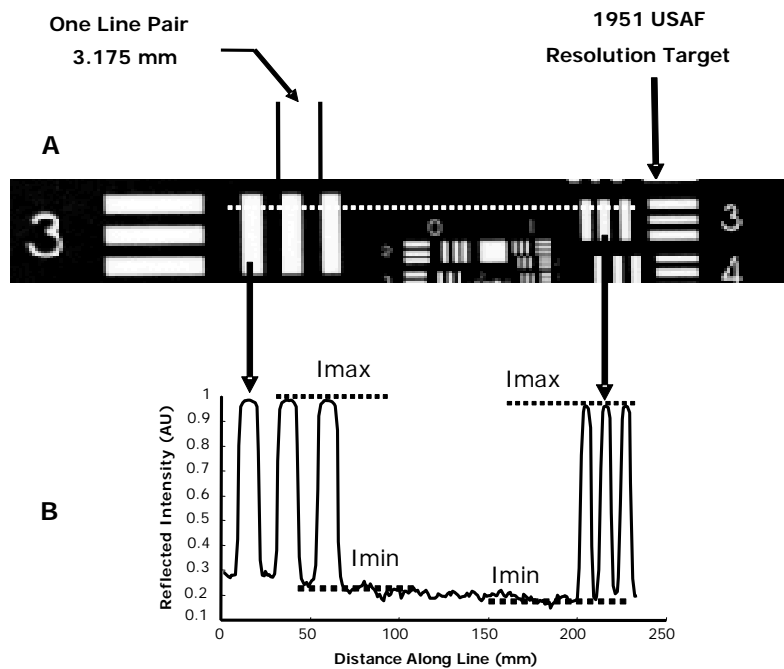


Figure 35, (A).1951 USAF resolution target. (B) Reflected Intensity plotted for the dotted line in (A).

A 1951 Quartz USAF (Edmund Optics, Barrington, NJ) resolution target depicted in Figure 35 where **A** depicts a portion of the target and the corresponding reflected intensity taken along a row of pixels is depicted in **B** was used to determine the spatial resolution. Generally, the spatial frequency, or number of line pairs, in which a line pair is defined as one white and one dark bar, increases (the number of pairs/unit length) as the percent contrast decreases [38]. The Quartz target was placed in the imaging path and a single image was collected which was then analyzed to determine the percent contrast by using equation (3). This procedure was followed for determining spatial resolution of the near infrared imaging as well as visible imaging system. Binning and magnification were changed keeping other experimental parameters the same and images were collected and analyzed to obtain the percent contrast. Percent Contrast calculations were done for the near infrared microscopic hyperspectral imaging system and plotted as a function of Spatial Resolving Power (mm) in Figure 36, the dependent variable, y , is Percent Contrast and the independent variable, x , is Spatial Resolution in millimeter and it is determined from the regression curve fit models when it cross the 20 % contrast threshold set by the Rayleigh criterion, blue dashed line. The PIXIS:400 BR FPA with a 1 x 1 binning employs the entire chip producing an image of 1340 x 400 pixels, depicted by diamonds, while squares represent a binning of 2 x 2, that employ 670 x 200 pixels. Similarly a binning of 3 x 3, 446 x 133 pixels, represented by triangles whereas 4 x 4 binning, 335 x 100, shown with crosses. From Figure Y, for a magnification of 10X and binning of 1 x 1 the regression equation is, $y = -725.67x^2 + 503.23x - 4.831$. Keeping the magnification same but changing the binning

to 2 x 2 the regression equation is, $y = -968.76x^2 + 629.96x - 25.402$. For a binning of 3 x 3 and 4 x 4 the respective regression equations are $y = -291.84x^2 + 467.47x - 29.796$ and $y = -635.83x^2 + 672.47x - 65.754$.

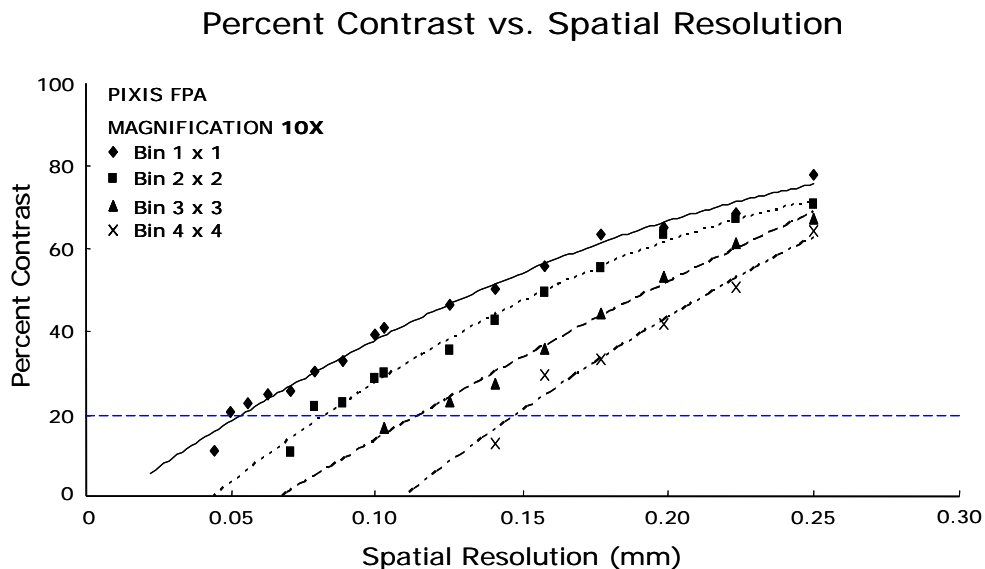


Figure 36, Spatial resolving power plot versus Percent contrast for PIXIS:400BR FPA and slit lamp magnification 10X.

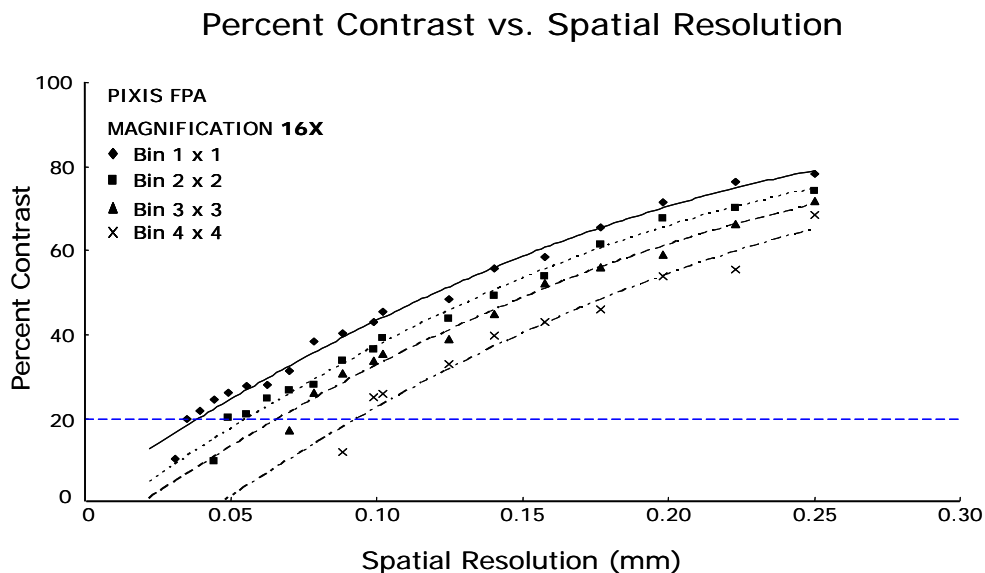


Figure 37, Spatial resolving power plot versus Percent contrast for PIXIS:400BR FPA and slit lamp magnification 16X.

Percent Contrast vs. Spatial Resolution

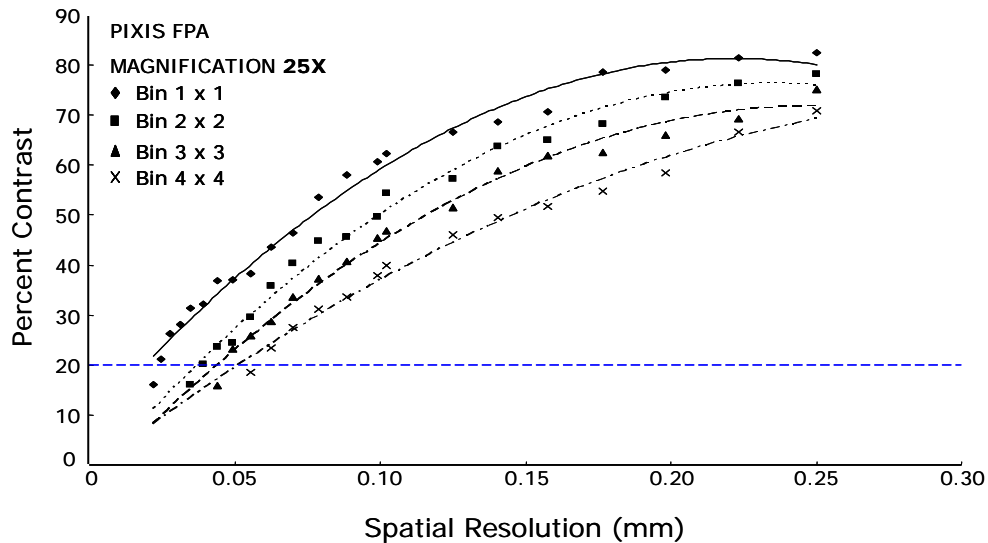


Figure 38, Spatial Resolution plot as a function of Percent contrast for PIXIS: 400BR FPA and slit lamp magnification 25X.

The spatial resolution for the system with the magnification at 10X is 0.054mm at binning 1 x 1, 0.083mm at binning 2 x 2, 0.115mm at binning 3 x 3 and 0.148mm for binning 4 x 4. Binning combines charges from adjacent pixels, for example in Figure 17 reducing a 4 pixel pattern for a binning of 2 x 2 to a single superpixel, thus losing the spatial resolution. This phenomenon of resolution being decreased with increased binning is displayed from the percent contrast numbers above.

Also if we keep the binning constant and examine the spatial resolution at different magnification we observe that at binning of 1 x 1 and magnification of 10X the resolution is 0.054 mm, whereas with magnification of 16X it is 0.051 mm and with 25X it is 0.019mm, Figure 37 and Figure 38. The slit lamp magnification which

increases from 10X, 16X to 25X, improves the spatial resolution, at the cost of the field of view. It also lowers the image brightness increasing the exposure times.

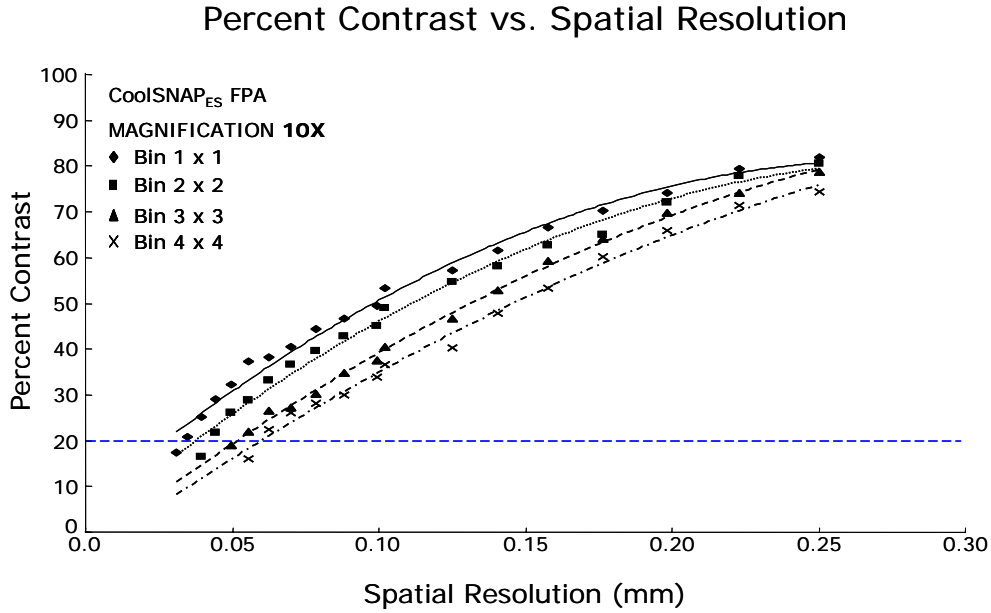


Figure 39, Spatial resolving power plot versus Percent contrast for CoolSNAP_{ES} FPA and slit lamp magnification 10X.

Similarly, Percent Contrast of the visible microscopic hyperspectral imaging system is plotted as a function of Spatial Resolving Power (mm) in Figure 39. Here each case shown below has a polynomial regression curve fit model. For a magnification of 10X and binning of 1 x 1, diamonds, the regression equation is, $y = -996.04x^2 + 548.86x + 5.7296$. Keeping the magnification same but changing the binning to 2 x 2, squares, the regression equation is, $y = -919.92x^2 + 544.64x + 0.8112$. For a binning of 3 x 3, triangles, and 4 x 4, crosses, the respective regression equations are $y = -660.48x^2 + 498.39x - 4.0232$ and $y = -531.26x^2 + 458.81x - 5.5901$. Again in

Percent Contrast vs. Spatial Resolution

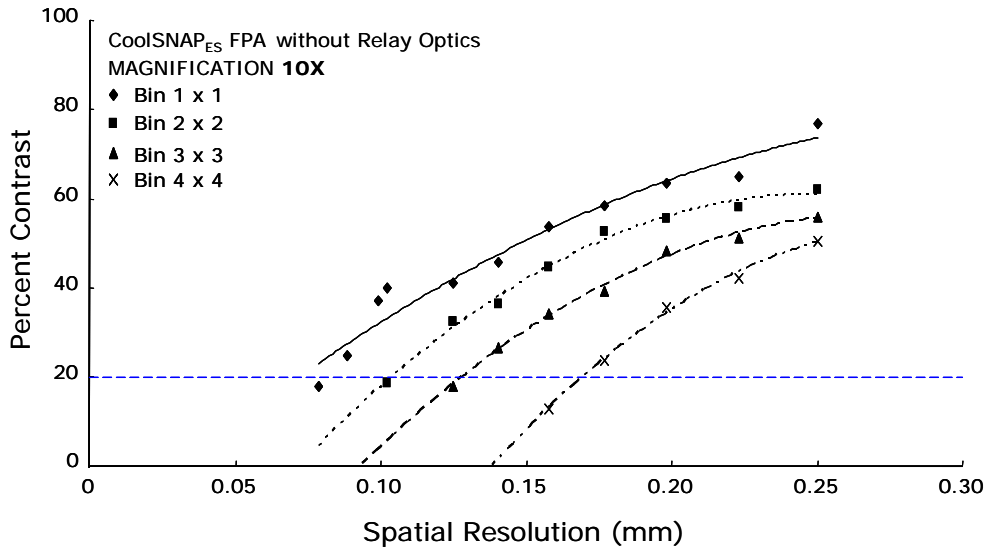


Figure 40, Spatial resolving power plot versus Percent contrast for CoolSNAP_{ES} FPA and slit lamp magnification 10X without the relay optics in the light path.

all the above cases, the dependent variable, y, is Percent Contrast and the independent variable, x, is Spatial resolution in millimeter and it is determined from the regression curve fit models when it cross the 20 % contrast threshold set by the Rayleigh criterion, blue dashed line. The spatial resolution for the visible hyperspectral imaging system with the magnification at 10X is 0.027mm at binning 1 x 1, 0.038mm at binning 2 x 2, 0.052mm at binning 3 x 3 and 0.06mm for binning 4 x 4. As mentioned before the binning decreases the spatial resolution which is proved from the spatial resolution numbers obtained.

Another interesting comparison was made using the visible microscopic hyperspectral imaging system by obtaining percent contrast measure for the visible system without the presence of the relay optics in the light path and plotted in Figure

40. Regression equations were obtained and analyzed keeping the Magnification 10X, and changing the binning on the FPA to find out the spatial resolution for system without the relay optic, yielding spatial resolutions of 0.072 mm for binning of 1 x 1, 0.104mm for binning of 2 x 2, 0.129 mm for binning 3 x 3 and 0.169 mm for binning 4 x 4. The spatial resolution was found to be worst then that for the system with relay optics in the light path. The relay optics were introduced in the system to increase the magnification of the system and allow the system to occupy larger area of the CCD chip thus improving the overall spatial resolution of the system as seen from the spatial resolution numbers for the system with and without the relay optics.

In all the experimentations, the reflected light creates an image onto the FPA of the microscopic hyperspectral system which is visually aligned onto the centre of the FPA using the image display in the V++ software. Figure 41 (A) shows a snapshot taken off the V++ software showing a misaligned image created on the FPA which is off from the centre of the imaging area while Figure 41 (B) shows the same image centered onto imaging area visually with the aid of V++ software.

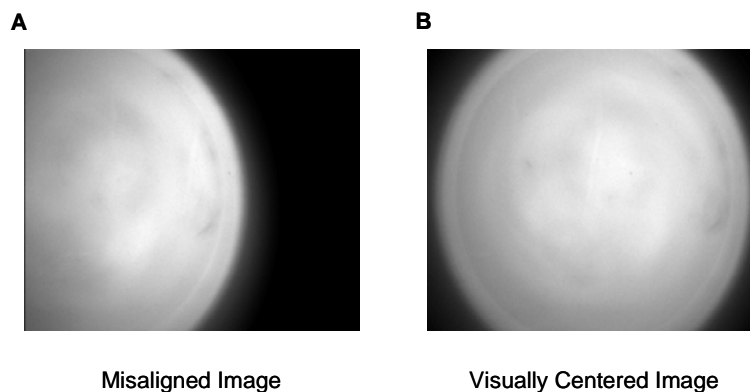


Figure 41, Image Alignment. A) Image off centre from the CCD chip. B) Visually aligned imaged onto the center of the CCD chip

3.2 System Performance

Hyperspectral imaging is emerging as a powerful imaging tool to exemplify spectral as well as the spatial characteristics. Microscopic Near infrared hyperspectral imaging system was used to image, non-invasively, microvascular perfusion of the dermal tissue, in-vivo, for assessing oxyhemoglobin contribution during resting condition for ten subjects. The hyperspectral data deconvoluted for the contribution of oxyhemoglobin is gray scale encoded, meaning the greater the pixel intensity the greater the oxyhemoglobin contribution as depicted by gray scale bar associated with an image.

The resting or the basal condition within the microvasculature perfusing the dermis of subject 1 is imaged to produce a gray scale image of oxyhemoglobin contributions, Figure 42A. As an example of the ability to determine oxyhemoglobin contribution from a given spatially resolved hyperspectral image, spectroscopic data from 140 detector pixels within the red box of Figure 42A, resting condition subject's dermal microvasculature, were averaged, yielding a high oxyhemoglobin contribution, as suggested by the overall high pixel intensities and their associated average measured spectrum, solid line in Figure 42B.

Similarly resting basal conditions hyperspectral image data was obtained from subject 2 and presented in Figure 43A. Spectroscopic information was obtained from 140 detector pixels under the area of the white box in Figure 43A and plotted as dotted line in Figure 43B. The spectroscopy strongly depicts the presence of deoxyhemoglobin which is also suggested by the lower oxyhemoglobin numbers and lower intensity of the

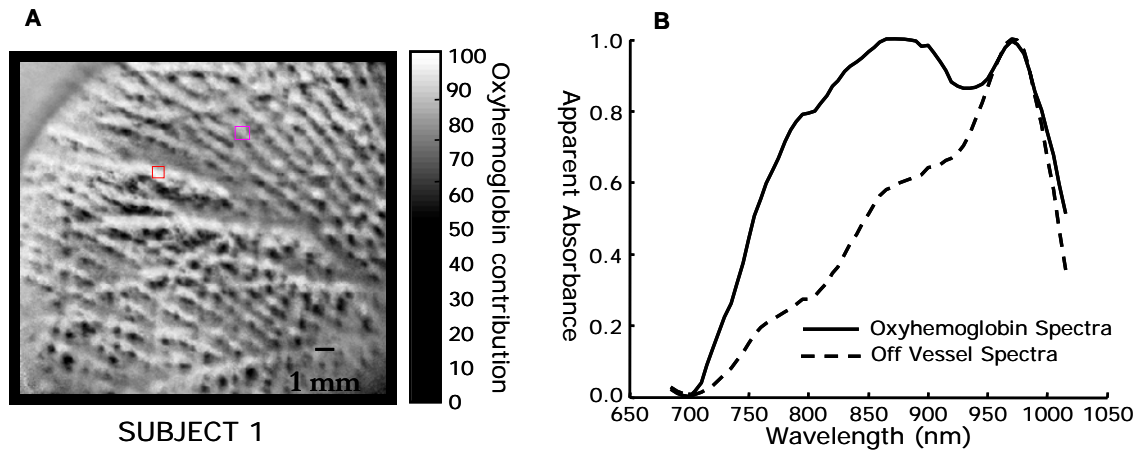


Figure 42, Near infrared Hyperspectral imaging. **A)** Gray scale encoded image depicting oxyhemoglobin contribution. **B)** Spectral output averaged over area under the boxes.

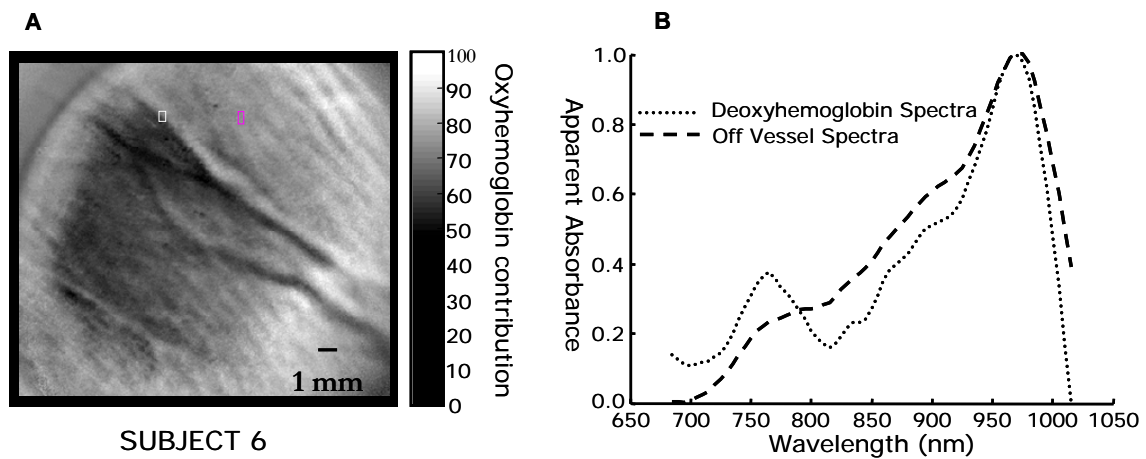


Figure 43, Near infrared Hyperspectral imaging. **A)** Gray scale encoded image visualized as oxyhemoglobin contribution. **B)** Spectral output averaged over the region under the boxes.

pixels in the image under the boxed region. In both the Figures 42 and Figure 43, dashed line represent spectral information obtained from underneath the region with the pink box having a classic water absorption spectral indicating no vessel is present in that region.

Table 5, Oxyhemoglobin contributions in Dermal tissue microvasculature

	Gender	Age	HbO ₂ Contribution over an assumed arterial region (Mean ± SEM)		Gender	Age	HbO ₂ Contribution over an assumed venous region (Mean ± SEM)
Subject 1	Male	23	87.65 ± 0.51	Subject 6	Male	27	64.18 ± 0.52
Subject 2	Male	24	87.49 ± 0.2	Subject 7	Male	23	55.27 ± 0.32
Subject 3	Male	24	91.53 ± 0.19	Subject 8	Male	23	65.23 ± 0.2
Subject 4	Male	23	88.46 ± 0.18	Subject 9	Male	25	65.13 ± 0.19
Subject 5	Male	23	94.82 ± 0.24	Subject 10	Male	25	62.68 ± 0.15

Ten subjects were imaged to obtain the oxyhemoglobin contributions within the dermis as shown in Table 5. The regions from under which the above average values evaluated were not random but visually selected depending on the spectroscopic information the region yielded. The red box region in subject 1, Figure 42 A, as per the spectroscopic information in Figure 42B is claimed to be highly oxygenated or arterial in nature and the value obtained under this red region is 87.65 % oxygenated further supports the claim. Similarly the white box region, Figure 43A, for subject 6 is assumed to be deoxygenated or venous in nature substantiated from the 64 % oxygenated obtained from below the boxed region.

The imaging of the dermal microvasculature with the help of the microscopic near infrared hyperspectral imaging system was a proof of principle example to test the ability of the microscopic imaging system to obtain oxyhemoglobin contribution. The

microscopic hyperspectral system was further applied towards imaging the microvasculature structure present in the anterior region of the human eye, especially the sclera, which required imaging in the visible spectrum, 520 – 602 nm. A hyperspectral image cube was obtained using the visible slit lamp microscopic imaging system, with experimental parameter such as magnification set to 10X, binning set to 2 x 2 and wavelength range 520 – 602 nm, incrementing at 2nm. These parameters

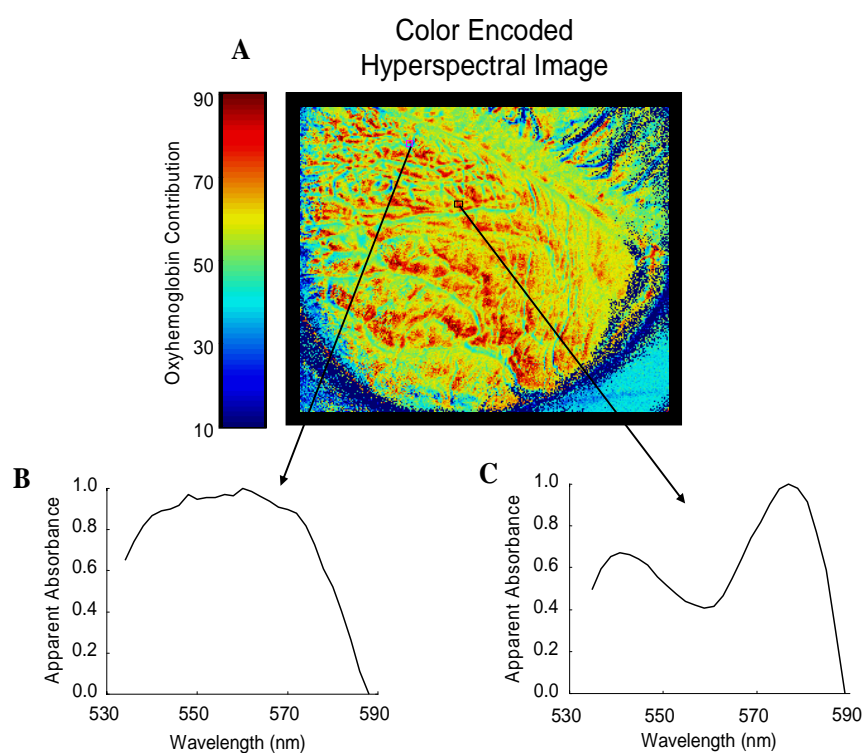


Figure 44, Microscopic hyperspectral imaging of the eye. A) Color encoded image showing oxyhemoglobin contribution values as a function of space. B) Spectral analysis from the pink box region resembling deoxyhemoglobin reference curve C) Spectral output over the black box region resembling strong oxyhemoglobin reference curve.

successfully reduced the acquisition time for the hyperspectral image cube to within 5 seconds which is critical for imaging the eye since the subject involved in the data

collection are not allowed to blink or move their eye since that would create artifacts in the images.

The hyperspectral cube was deconvoluted for oxyhemoglobin contribution values that are color encoded and spatially depicted in Figure 44A above. A small region over a high oxyhemoglobin contribution region, black box, as suggested from the colorbar, red areas, was selected and pixels under the region were averaged to obtain a spectrum shown in Figure 44C which resembles the oxyhemoglobin spectrum. Similarly the spectrum under the area of the pink box, Figure 44B, represents a deoxyhemoglobin spectrum.

Table 6, Oxyhemoglobin contributions in Scleral surface microvasculature

	Gender	Age	HbO ₂ Contribution over an assumed arterial region (Mean ± SEM)	HbO ₂ Contribution over an assumed venous region (Mean ± SEM)
Subject1	Male	27	65.86 ± 1.5	52.32 ± 1.66
Subject2	Female	24	66.69 ± 0.55	52.33 ± 0.65
Subject3	Male	37	65.87 ± 0.57	58.74 ± 1.41
Subject4	Male	23	68.06 ± 0.78	47.93 ± 0.96
Subject5	Male	25	67.63 ± 1.1	51.9 ± 1.38
Subject6	Male	23	69.39 ± 0.99	52.99 ± 1.17
Subject7	Male	25	69.1 ± 0.87	58.35 ± 1.33

Seven healthy subjects were imaged to obtain scleral tissue oxyhemoglobin contributions for assumed arterial and venous structures in the image as displayed by the spectroscopic information. The average oxyhemoglobin contribution values for these seven subjects are displayed in Table 6. The regions from under which the above

average values evaluated were not random but visually selected depending on the spectroscopic information the region yielded.

The values in Table 5 and Table 6 are qualitative values with quantitative evaluations pending. These values demonstrate that there exist marked differences between arterial and venous structure oxyhemoglobin contributions and that the system is capable of distinguishing between arterial and venous structure in the tissue being imaged.

CHAPTER 4

DISCUSSION

Hyperspectral Imaging, a blend between spectroscopy and imaging, is a relatively new technology that is finding novel and diverse applications in the field of medical diagnosis. A multi-modal, novel microscopic Hyperspectral imaging system using a slit lamp microscope was developed that could render its usefulness clinically in various medical diagnostic applications.

4.1 Microscopic Near Infrared Hyperspectral Imaging system

Slit lamp microscope, near infrared LCTF, and the PIXIS: 400BR focal plane array were integrated with the help of beam splitter, relay optics and the camera lens to form the microscopic near infrared Hyperspectral system. These components were characterized for optimal working of the system. The slit lamp is an optical instrument similar to a simple microscope that provides high magnification, but with a binocular vision and functioning with its own illumination system that can be adjusted. The slit lamp source intensity and temperature were characterized, to find out that there was no significant increase in temperature at the intensity used in the experimental conditions which rendered its safety in avoiding thermal injuries due to near infrared light. The

beam splitter attached to the slit lamp makes it possible to shine reflected light from the subject onto a relay optic that focuses it onto an electronic tunable filter, the LCTF that distinguishes light into individual wavelengths. The LCTF was characterized was firstly calibrated to make sure the desired wavelength being entered via the computer is actually what the LCTF gets tuned to. Next spectral resolution, average spectral resolution being 6.45 nm for the spectral range of our application, 685 nm –1015 nm, and tune–delay time were characterized, with a tune-delay time of 50ms. The spectral resolution of the LCTF makes it possible to use it for deconvoluting the oxyhemoglobin and deoxyhemoglobin spectrum that is spectrally broader than the highest spectral resolution of the LCTF. The tune-delay or tune-wait time renders it usefulness, reducing noise in the output when it is included in the software for controlling the automation of the data acquisition process.

The focal plane array, PIXIS: 400BR, a 1340 x 400 array provides better quantum efficiency driving improved image quality in the NIR region. The spatial resolving power, which refers to the minimum distance between line pairs that can be detected, was characterized coupled with various binning and magnification settings available. The PIXIS: 400BR FPA binned at 1 x 1, with the near infrared LCTF in the optical path tuned to 750nm and a magnification 10X, has a spatial resolution of 0.054 mm as compared to 0.35 mm for the macroscopic hyperspectral system that included the CoolSNAP_{ES} CCD with the high resolution LCTF in the path, being tuned to 645 nm [46]. This better resolution in spite of the fact that, PIXIS:400BR has larger pixel size than the CoolSNAP_{ES} can be linked to the relay optics filling up the CCD chip and

the slit lamp microscope magnification. As mentioned earlier magnification increases the spatial resolution of the system whereas binning reduces it. The high spatial resolution obtained with different parameters of the system makes it feasible to image smaller capillary beds present in the microvasculature of the tissue.

Finally after achieving all this experimental parameter the system was used to examine microvascular perfusion in the dermal microvasculature of the palmar region, as a proof of principle. The human circulatory system is the major source of blood distribution to the body tissues. An adequate amount of blood supply is necessary for the tissues since they derive the required amounts of oxygen and nutrients required for normal functioning from the blood. The majority exchange of oxygen and nutrients takes place in the microvasculature of the tissue [47-49]; however currently used widespread clinical technology assesses blood from the major vessels either prior to, arterial, or after, venous, that has already perfused through the microvasculature or from a single point measure such as the finger, in case of Pulse Oximetry. This Hyperspectral imaging technique with the help of recent advancements in liquid crystal, silicon wafer technology and ever increasing faster computing capabilities have made it probable to evaluate the contribution of oxyhemoglobin perfusing the microvasculature of the tissue; thus making it possible to differentiate poorly perfused tissue and well perfused tissue on basis of the oxyhemoglobin contributions [3, 36, 38, 50, 51].

Microscopic imagery of the dermal tissue was acquisitioned for a series of wavelengths that are stacked, forming a hyperspectral image data cube which consists of one spectral and two spatial dimensions. Spectroscopic analysis, deconvolution,

associated with each detector pixel takes place with the help of at least two reference spectra, oxy- and deoxyhemoglobin using a multivariate least-squares approach; resulting in gray scale encoded images that reflect spatial distribution of oxyhemoglobin contribution.

4.2 Microscopic Visible Hyperspectral Imaging system

After demonstrating capabilities of the microscopic hyperspectral imaging system using dermal microvasculature imaging as a proof of principle, we turn our focus onto the major application, Imaging of the Human eye, especially the Sclera. The sclera is the white portion of the eye, covered by the Episclera, tenon's capsule, and the conjunctiva [52]. The blood vessels seen on the scleral surface actually are found between these various regions. Scleral disease such as scleritis and episcleritis, are uncommon in ophthalmology patients, however they present symptoms for serious, painful and life threatening systemic diseases such as Rheumatoid Arthritis, Syphilis, Spondylitis etc [53].

The anterior region of the human eye was imaged using the microscopic visible hyperspectral imaging system. The visible system uses the CoolSNAP_{ES} CCD in conjunction with the visible low resolution LCTF and the slit lamp microscope. The CoolSNAP_{ES} CCD's spatial resolving power at a binning of 2 x 2 and a magnification of 10X is 0.038mm is better than the resolving power of the PIXIS: 400BR with the same parameters being 0.083mm. Since speed is an important trade off with the imaging of the eye the 20 MHz readout rate is preferred against 2 MHz readout rate of

the PIXIS FPA. Also to decrease the acquisition time of the system the spectral range and spectral resolution were reduced to 520 – 602nm and increments of 2 nm, instead of the previously reported macroscopic version of the visible hyperspectral system developed here at UTA that used a spectral range of 520 – 645 nm, with the increment of 1nm. These were the two major trade off's considered to reduce the data acquisition time to 5 seconds that is clinically suitable for eye imaging applications. Inputting these experimental parameters with the slit lamp magnification set to 10X, sclera of the subject was imaged to obtain a hyperspectral data cube that upon deconvolution with the visible range reference spectra of oxyhemoglobin and deoxyhemoglobin rendered an image that contained spatially distributed contributions of oxyhemoglobin.

CHAPTER 5

CONCLUSIONS AND FUTURE GOALS

The Multi-modal Microscopic HyperSpectral Imaging System was integrated and characterized to obtain oxyhemoglobin contributions perfusing the microvasculature, non-invasively and in vivo. A proof of principle study that involved clinical modeling of the dermal tissue for vascular occlusion and reperfusion was successfully undertaken and vascular changes associated were recorded. Further, the sclera of the human eye was imaged to depict oxyhemoglobin contributions in the microvascular vessels perfusing the tissue of the human eye.

The system can be further optimized, with usage of better magnification and focusing optics, to utilize the full focal plane array chip since currently it uses 600 x 400 pixels instead of 1392 x 1040 pixels for the CoolSNAPES and 1340 x 400 pixels in the PIXIS FPA, which will increase the spatial resolution of the system. Movement artifacts within the subject eye occurring due to sudden eye movements are generally hard to control; hence efforts are necessary to develop software that provides movement artifact free hyperspectral eye images.

Currently, plans are underway to translate this system in a clinical setting at an ophthalmology clinic at UT Southwestern to image the vasculature of the human retina. Future goals include using this retinal imaging technique as a toll for early diagnosis of vascular eye abnormalities such as diabetic retinopathy, glaucoma.

APPENDIX A

UTA SUBJECT CONSENT FORM - DERMAL



INFORMED CONSENT

PRINCIPAL INVESTIGATOR: Bhavesh Shah

TITLE OF PROJECT: In-vivo Microvasculature Visualization using Hyperspectral Imaging

This Informed Consent will explain about being a research subject in an experiment. It is important that you read this material carefully and then decide if you wish to be a volunteer.

PURPOSE:

The purpose of this research study is to develop a noninvasive microscopic hyperspectral imaging method to image the contribution of inherent blood constituents perfusing the skin. The Hyperspectral imaging method is a novel noninvasive imaging modality that uses light, to measure the contribution of inherent blood constituents. The objective of this project will be to acquire HyperSpectral imaging data from skin of your palm by shining light, noninvasively and in-vivo, and calculate the contribution of inherent blood constituents.

DURATION

This research project is being done under the supervision of Dr. Karel Zuzak, Ph.D., at UT Arlington where the protocol will be carried out. The study will consist of 10 subjects. The expected duration for the study is approximately 50 minutes for a single subject.

PROCEDURES

You as a subject will be asked to visit the Laboratory of Biomedical Imaging, once in the laboratory and after signing the consent form, you will be seated and relaxed for 10 minutes. Then resting systolic and diastolic blood pressure readings will be taken using a standard sphygmomanometer, after which you will again relax for 30 minutes. Normal room light will be turned off and the skin tissue of interest, within the palm of

the hand will be marked using a standard office marker. This mark will act as a spatial reference to control/ensure that the spatial location of the tissue being imaged does not change. The tissue of interest will be illuminated with light from a standard clinical slit lamp, used in Ophthalmology clinics routinely for eye examinations, for 30 seconds while acquiring the Hyperspectral images. Then vascular occlusion will be modeled by inflating the blood pressure cuff around your arm to 10% above the resting systolic pressure for one minute. While the cuff is inflated, the marked region on your palm will be illuminated by the slit lamp source for 30 seconds and hyperspectral images will be collected. Reperfusion will be modeled by releasing the cuff pressure. Three minutes after the sphygmomanometer pressure reading falls below diastolic pressure, the marked region in your palm will be imaged for a period of 30 seconds. The project uses a noninvasive imaging modality, Hyperspectral Imaging, in order to determine the contribution of inherent blood constituents. We are using a standard clinical Slit Lamp (Marco G2, Universal Ophthalmic Equipment) that is usually used for eye examination. The filter

PRINCIPAL INVESTIGATOR: Bhavesh Shah

TITLE OF PROJECT: In-vivo Microvasculature Visualization using Hyperspectral Imaging

(Liquid Crystal Tunable Filter,LCTF, Cambridge Research and Instrumentation) and the detector (CCD, PIXIS 400BR, Princeton Instrument) combining the hyperspectral system are integrated with the microscope to acquire hyperspectral image cubes noninvasively and in-vivo. Briefly the light focussed by the slit lamp on the subject's palm gets reflected from the subject's skin surface and is captured by a digital camera, forming a series of images, that are spectrally and statistically analysed using computer software, to determine the contributions of inherent blood constituents without touching the skin.

POSSIBLE RISKS/DISCOMFORTS

Measuring blood pressure and inflating the blood pressure cuff 10% above the systolic pressure may create some discomfort. The standard clinical slit lamp provides the lamp source for illuminating the skin. This source is a broad band source that contains visible and near infrared light; however the slit lamp along with its illumination source is routinely used in Ophthalmology clinics for routine eye examinations. In addition we have measured no significant temperature increase using this source for the experimental conditions employed for this study, thus no possibility of heating the skin.

Briefly, the instrumentation consists of a source, very similar to a bright table lamp and a digital camera. As in a photo studio, there is a potential risk of you accidentally tripping over the equipment. Proper instructions will be given to you about the safety procedures that need to be followed during the experiment.

Otherwise, there are no potential risks (psychological, social, legal, and confidentiality) to you, as a subject of this study. However; you should not participate in the study if you have any pulmonary or cardiac abnormalities or any other serious medical condition

that will interfere with the conduct of the study. Female subjects that are pregnant or could become pregnant, lactating, menopausal, or are experiencing an abnormal menstruation should not participate in the study.

POSSIBLE BENEFITS

There are no potential benefits to the study subject. However, it is hoped that the information learned from this study will help clinicians and scientists image the contribution of inherent blood constituents noninvasively and in-vivo. The proposed research may also provide a useful method to monitor the contribution of inherent blood constituents during clinical and surgical procedures on a microscopic level. None of the subject, will be compensated for their participation in the study. Students will not receive course credit for participating as subjects in the study.

PRINCIPAL INVESTIGATOR: Bhavesh Shah

TITLE OF PROJECT: In-vivo Microvasculature Visualization using Hyperspectral Imaging

ALTERNATIVE PROCEDURES / TREATMENTS

You as a subject, can withdraw from participating in the study at any point without any consequences.

CONFIDENTIALITY

Every attempt will be made to see that your study results are kept confidential. Names will be removed from all specimens, forms, documents and communication and will be replaced by identifier numbers. The Coded charts, test results, study casebooks, etc. will

be kept in the Laboratory of Principle Investigator under lock and key for at least three (3) years after the end of research. Digital raw data measured by the instrumentation will be identified by the corresponding identifier number and stored within a secure section of a hard drive located in the office of the Principle Investigator. The results of this study may be published and/or presented at meetings without naming you as a subject. Although your rights and privacy will be maintained, the Secretary of the Department of Health and Human Services, the UTA IRB, the FDA (if applicable), and personnel particular to this research i.e. Bhavesh Shah (Principal Investigator), Dr. Karel Zuzak (Co-Investigator and Supervising professor), and Dr. Khosrow Behbehani (Co-Investigator and Bioengineering department chair) will have access to the study records. Your records will be kept completely confidential according to current legal requirements. They will not be revealed unless required by law, or as noted above.

COMPENSATION FOR MEDICAL TREATMENT:

The University of Texas at Arlington (UTA) will pay the cost of emergency first aid for any injury that occurs as a result of your participation in this study. UTA will not pay for any other medical treatment. Claims against UTA or any of its agents or employees may be submitted according to the Texas Tort Claims Act (TTCA). These claims may be settled to the extent allowable by state law as provided under the TTCA, (Tex. Civ. Prac. & Rem. Code, secs. 101.001, et seq.). For more information about claims, you may contact the Chairman of the Institutional Review Board of UTA at 817/272-1235.

FINANCIAL COSTS

There is no financial cost to you as a participant. You as a subject, will not be compensated for your participation in the study.

PRINCIPAL INVESTIGATOR: Bhavesh Shah

TITLE OF PROJECT: In-vivo Microvasculature Visualization using Hyperspectral Imaging

CONTACT FOR QUESTIONS

If you have any questions, problems or research-related medical problems at any time, you may call Bhavesh Shah at 817-272-0809, or Dr. Karel Zuzak at 817-272-7318. You may call the Chairman of the Institutional Review Board at 817-272-1235 for any questions you may have about your rights as a research subject.

VOLUNTARY PARTICIPATION

Participation in this research experiment is voluntary. You may refuse to participate or quit at any time. You may quit by calling, Bhavesh Shah, whose phone number is 817-272-0809. You will be told immediately, if any of the results of the study should reasonably be expected to make you change your mind about staying in the study. By signing below, you confirm that you have read or had this document read to you. You will be given a signed copy of this informed consent document. You have been and will continue to be given the chance to ask questions and to discuss your participation with the investigator.

You freely and voluntarily choose to be in this research project.

PRINCIPAL INVESTIGATOR: _____ DATE

SIGNATURE OF VOLUNTEER DATE

SIGNATURE OF PATIENT/LEGAL GUARDIAN (if applicable) DATE

SIGNATURE OF WITNESS (if applicable)

APPENDIX B

UTA SUBJECT CONSENT FORM - HUMAN EYE



INFORMED CONSENT

PRINCIPAL INVESTIGATOR: Bhavesh Shah

TITLE OF PROJECT: In-vivo Microvasculature Visualization using Hyperspectral Imaging

This Informed Consent will explain about being a research subject in an experiment. It is important that you read this material carefully and then decide if you wish to be a volunteer.

PURPOSE:

The purpose of this protocol is to develop a method to visualize the percentage of inherent blood chromophores in the anterior region of the eye using the noninvasive microscopic hyperspectral imaging modality. The Hyperspectral imaging method is a novel noninvasive imaging modality that uses light, to measure the percentage of inherent blood constituents. The objective of this project, is to acquire Hyperspectral Imaging data from the anterior region of the eye, noninvasively and in-vivo, and calculate the percentage of inherent blood chromophores using a standard clinical eye examining slit lamp microscope.

DURATION

This research project is being done under the supervision of Dr. Karel Zuzak, Ph.D., at UT Arlington where the protocol will be carried out. The study will consist of 10 subjects. The expected duration for the study is approximately 15 minutes for a single subject.

PROCEDURES

You as a subject will be asked to visit the Laboratory of Biomedical Imaging, once in the laboratory and after signing the consent form, you will be seated and relaxed for 10 minutes. You as a subject will then be asked to place your chin onto the chin rest

attached to the standard clinical slit lamp, used in Ophthalmology clinics routinely for eye examinations. The anterior region of the eye will be illuminated using the light from the slit lamp for 5 seconds while acquiring a series of digital images/pictures - Hyperspectral images. The project uses a noninvasive imaging modality, Hyperspectral Imaging, in order to determine the percentage of inherent blood chromophores. We are using a standard clinical Slit Lamp (Marco G2, Universal Ophthalmic Equipment) that is usually used for eye examination. The filter (Liquid Crystal Tunable Filter, LCTF, Cambridge Research and Instrumentation) and the detector (CCD, CoolsnapES ,Princeton Instrument) combining the hyperspectral system are integrated with the microscope to acquire series of digital image/pictures forming a hyperspectral image cube, noninvasively and in-vivo. Briefly the light focussed by the slit lamp on the subject's eye is captured by a digital camera when it gets reflected from the subject's eye surface, forming a series of images, that are spectrally and statistically analysed using computer software, to determine the the percentage of inherent blood chromophores without touching the eye.

PRINCIPAL INVESTIGATOR: Bhavesh Shah

TITLE OF PROJECT: In-vivo Microvasculature Visualization using Hyperspectral Imaging

POSSIBLE RISKS/DISCOMFORTS

While the images are being captured you as the subject will be asked, not to blink and to focus at a point, in order to minimize eye movements and ultimately limit motion artifacts in the images, which you may find to be inconvenient.

The standard clinical slit lamp provides the lamp source for illuminating the eye. This source is a broad band source that contains visible and near infrared light; however the slit lamp along with its illumination source is routinely used in Ophthalmology clinics for routine eye examinations. In addition we have measured no significant temperature increase using this source for the experimental conditions employed for this study, thus no possibility of heating or thermal damage.

Briefly, the instrumentation consists of a source, very similar to a bright table lamp and a digital camera. As in a photo studio, there is a potential risk of you accidentally tripping over the equipment. Proper instructions will be given to you about the safety procedures that need to be followed during the experiment.

Otherwise, there are no potential risks (psychological, social, legal, and confidentiality) to you, as a subject of this study. However; you should not participate in the study if you have any pulmonary or cardiac abnormalities or any other serious medical condition that will interfere with the conduct of the study. Female subjects that are pregnant or could become pregnant, lactating, menopausal, or are experiencing an abnormal menstruation should not participate in the study.

POSSIBLE BENEFITS

There are no potential benefits to the study subject. However, it is hoped that the information learned from this study will help clinicians and scientists image the percentage of inherent blood chromophores noninvasively and in-vivo. The proposed research may also provide a useful method to monitor percentage of blood chromophores such as oxyhemoglobin, which is important in eye diseases such as cataract, diabetic retinopathy etc. None of the subject, will be compensated for their participation in the study. Students will not receive course credit for participating as subjects in the study.

ALTERNATIVE PROCEDURES / TREATMENTS

You as a subject, can withdraw from participating in the study at any point without any consequences.

PRINCIPAL INVESTIGATOR: Bhavesh Shah

TITLE OF PROJECT: In-vivo Microvasculature Visualization using Hyperspectral Imaging

CONFIDENTIALITY

Every attempt will be made to see that your study results are kept confidential. Names will be removed from all specimens, forms, documents and communication and will be replaced by identifier numbers. The Coded charts, test results, study casebooks, etc. will

be kept in the Laboratory of Principle Investigator under lock and key for at least three (3) years after the end of research. Digital raw data measured by the instrumentation will be identified by the corresponding identifier number and stored within a secure section of a hard drive located in the office of the Principle Investigator. The results of this study may be published and/or presented at meetings without naming you as a subject. Although your rights and privacy will be maintained, the Secretary of the Department of Health and Human Services, the UTA IRB, the FDA (if applicable), and personnel particular to this research i.e. Bhavesh Shah (Principal Investigator), Dr. Karel Zuzak (Co-Investigator and Supervising professor), and Dr. Khosrow Behbehani (Co-Investigator and Bioengineering department chair) will have access to the study records. Your records will be kept completely confidential according to current legal requirements. They will not be revealed unless required by law, or as noted above.

COMPENSATION FOR MEDICAL TREATMENT:

The University of Texas at Arlington (UTA) will pay the cost of emergency first aid for any injury that occurs as a result of your participation in this study. UTA will not pay for any other medical treatment. Claims against UTA or any of its agents or employees may be submitted according to the Texas Tort Claims Act (TTCA). These claims may be settled to the extent allowable by state law as provided under the TTCA, (Tex. Civ.

Prac. & Rem. Code, secs. 101.001, et seq.). For more information about claims, you may contact the Chairman of the Institutional Review Board of UTA at 817/272-1235.

FINANCIAL COSTS

There is no financial cost to you as a participant. You as a subject, will not be compensated for your participation in the study.

CONTACT FOR QUESTIONS

If you have any questions, problems or research-related medical problems at any time, you may call Bhavesh Shah at 817-272-0809, or Dr. Karel Zuzak at 817-272-7318. You may call the Chairman of the Institutional Review Board at 817-272-1235 for any questions you may have about your rights as a research subject.

PRINCIPAL INVESTIGATOR: Bhavesh Shah

TITLE OF PROJECT: In-vivo Microvasculature Visualization using Hyperspectral Imaging

VOLUNTARY PARTICIPATION

Participation in this research experiment is voluntary. You may refuse to participate or quit at any time. You may quit by calling, Bhavesh Shah, whose phone number is 817-272-0809. You will be told immediately, if any of the results of the study should reasonably be expected to make you change your mind about staying in the study. By signing below, you confirm that you have read or had this document read to you. You will be given a signed copy of this informed consent document. You have been and will continue to be given the chance to ask questions and to discuss your participation with the investigator.

You freely and voluntarily choose to be in this research project.

PRINCIPAL INVESTIGATOR: _____ DATE

SIGNATURE OF VOLUNTEER DATE

SIGNATURE OF PATIENT/LEGAL GUARDIAN (if applicable) DATE

SIGNATURE OF WITNESS (if applicable)

REFERENCES

1. Gat N. Imaging Spectroscopy Using Tunable Filters: A Review. SPIE, 2000; 4056: 50-64.
2. Motta G, Rizza F, Storer JA. Hyperspectral Data Compression. NY: Springer Publication, 2006.
3. Zuzak KJ, Schaeberle MD, Gladwin MT, Cannon RO 3rd, Levin IW. Noninvasive determination of spatially resolved and time-resolved tissue perfusion in humans during nitric oxide inhibition and inhalation by use of a visible-reflectance hyperspectral imaging technique. *Circulation*. 2001; 104:2905-2910.
4. Tuan Vo-Dinh. A Hyperspectral imaging system for in vivo optical diagnostics. *Engineering in Medicine and Biology Magazine, IEEE*. 2004; 23:40- 49.
5. Ferris DG, Lawhead RA, Dickman E, et al. Multimodal Hyperspectral Imaging for the Noninvasive Diagnosis of Cervical Neoplasia. *Journal of Lower Genital Tract Disease* 2001; 5:65-72.
6. Monteiro ST, Kosugi YU, Watanabe E. Towards Applying hyperspectral Imagery as an Intraoperative Visual Aid Tool. Proc. 4th VIIP, Marbella, Spain. 2004; 483-488.

7. Stranc MF, Sowa MG, Abdulrauf B, Mantsch HH. Assessment of tissue viability using near-infrared spectroscopy. *British Journal of Plastic Surgery*. 1998; 51:210-217.
8. Website - <http://www.infoplease.com/ce6/sci/A0823316.html>.
9. Website - <http://tutor.lscf.ucsb.edu/instdev/sears/biochemistry/>
10. Website - <http://www.nlm.nih.gov/medlineplus/ency/article/003645.htm>
11. Mader SS, *Inquiry into Life*. Dubuque: W.C. Brown, 1985.
12. Dickerson RE, Geis I. *Hemoglobin: structure, Function, Evolution, and pathology*. California: The Benjamin/Cummings Publishing company, Inc., 1983.
13. Maclean N. *Hemoglobin, The Institute of Biology's studies in biology*, Vol: 93. London: Arnold, 1978.
14. Website - <http://en.wikipedia.org/wiki/Oxyhemoglobin>
15. Dave T. Advice on choosing the right Slit Lamp. *Optometry Today*. 2004, April; 37 – 40.
16. Henson DB. *Optometric instrumentation*. Boston: Butterworth-Heinemann, 1996.
17. Ledford JK, Sanders VN. *The slit lamp primer*. NJ: SLACK, Inc., 1998.

18. Website - http://marco.com/pdfs/Ultra_SL_Broch.pdf.
19. Website - http://www.cri-inc.com/files/VariSpec_Brochure.pdf
20. Website - <http://www.cri-inc.com/products/components.asp>
21. Slawson RW, Ninkov Z, Horch EP. Hyperspectral Imaging: Wide-Area Spectrophotometry Using a Liquid Crystal Tunable Filter. *PASP*. 1999; 111: 621 – 626.
22. Morris HR, Hoyt CC, Treado PJ. Imaging Spectrometers for Fluorescence and Raman Microscopy: Acousto-Optic and Liquid Crystal Tunable Filters. *Applied Spectroscopy*. 1994; 48: 857 – 866.
23. Miller PJ. Use of Tunable Liquid Crystal Filters to Link Radiometric and Photometric Standards. *Metrologia*. 1991; 28: 145 – 149.
24. Call J, Lodder RA. Application of a Liquid Crystal Tunable Filter to Near-Infrared Spectral Searches. *Proceedings of SETICon 02*. April 26-28, NJ, 2002.
25. LCTF User Manual, Cambridge Research and Instrumentation.
26. Website
http://www.nikonians.org/html/resources/nonikon_articles/tokina/Tokina_ATX_M100AF/Tokina_AT-X_M100AF_2.html
27. PIXIS system User Manual, Princeton Instruments.

28. <http://content.piaction.com/Uploads/Princeton/Documents/Datasheets/PIXIS/PIXIS%20400%20Rev%20B0.pdf>
29. Etaloning in Back Illuminated CCD's. Roper Scientific Inc.,
(Source: <http://content.piaction.com/Uploads/Princeton/Documents/Whitepapers/etaloning.pdf>)
30. Website - <http://www.photomet.com/coolsnap.html>
31. CoolSNAP Interline Camera, Roper Scientific Inc.,
(Source: <http://www.piaction.com/pdfs/whitepapers/interline.pdf>)
32. CoolSNAP_{ES} CCD User Manual, Roper Scientific.
33. Website - http://www.photomet.com/software_pvcam.html
34. Getting Started with V++, User manual, Digital Optics Ltd.
35. Shaw RA, Mansfield JR, Kupriyamov VV, Mantsch HH. In vivo optical/near-infrared spectroscopy and imaging of metalloproteins. J. Inorg. Biochem. 2000;79:285-93
36. Leonardi L, Sowa MG, Payette JR, Mantsch HH. Near infrared spectroscopy imaging: A new approach to assess burn injuries. Am. Clin. Lab. 2000; 19:20-22.
37. Mark Cope. The Application of near infrared spectroscopy to non-invasive monitoring of cerebral oxygenation in the newborn infants. London: University College, 1991.
(Source: <http://www.medphys.ucl.ac.uk/research/borl/homepages/mcope/>)

38. Zuzak KJ, Schaeberle MD, Lewis EN, Levin IW. Visible Reflectance Hyperspectral Imaging: Characterization of a Noninvasive, in Vivo System for Determining Tissue Perfusion. *Anal. Chem.*2002;74:2021-2028.
39. Kortum G. *Reflectance Spectroscopy, Principles, Methods, Applications*. NY: Springer-Verlag New York Inc., 1969.
40. Hajizadesaffar M, Feather JW, Dawson JB. An investigation of factors affecting the accuracy of in vivo measurements of skin pigments by reflectance spectrophotometry. *Phys Med Biol.*1990; 35:1301–15.
41. Knoefel WT, Kollias N, Rattner DW, et al. Reflectance spectroscopy of pancreatic microcirculation. *J Appl. Physiol.*1996; 80:16-23.
42. Springsteen. A. Standards for reflectance measurements. *Spectroscopy.* 2000; 15:20-27.
43. Press WH, Flannery BP, Teukolsky SA, Vetterling WT. *Numerical Recipes in C: The Art of Scientific Computing*. NY: Cambridge University Press, 1992.
44. Beebe KR, Kowalski BR. An Introduction to Multivariate Calibration and Analysis. *Anal. Chem.*1987; 57:1007A – 1017A.
45. Website-
http://www.iscienceproject.com/labs/pdf_labs/6355_lidcaysdistance.pdf
46. Website - <http://www.dscp.dla.mil/GI/general/lightcat/Cookecal.pdf>

47. Kothare A. Visible reflectance hyperspectral imaging system with improved capabilities for translational medicine projects. University of Texas at Arlington, 2005.
48. Li, John K-J. Dynamics of the Vascular System. Series on Bioengineering and Biomedical Engineering; V. 1. River Edge: NJ World Scientific Publishing Co., 2004.
49. Klabunde RE. Cardiovascular Physiology Concepts, Philadelphia; Lipincott Williams & Wilkins, 2005.
50. Berne RM, Levy MN. Principles of physiology. St. Louis: Mosby, 2000.
51. Zuzak KJ, Gladwin MT, R. O. Cannon 3rd, Levin IW. Imaging hemoglobin oxygen saturation in sickle cell disease patients using noninvasive visible reflectance hyperspectral techniques: effects of nitric oxide. Am. J. Physiol. Heart. Circ. Physiol.2003; 285:1183-9.
52. Siegemund M, Bommel JV, Ince C. Assessment of regional tissue oxygenation. Intensiv. Care. Med., 1999; 25:1044-60.
53. Watson PG, Hazleman BL. The sclera and systemic disorders. Philadelphia: B. Saunders Company, Ltd., 1976.
54. Website - <http://Articles/eMedicine> – Scleritis.

BIOGRAPHICAL INFORMATION

Bhavesh Shah, the author, has to his credit the Bachelor of Biomedical Engineering degree that he earned at Mumbai University, Mumbai, India, in August 2002. He joined University of Texas at Arlington in the fall 2003 semester, to pursue Masters Degree in Biomedical Engineering. Current research focus pertains to the work in the field of Medical Imaging, especially Hyperspectral Imaging. Other research inclinations include Cancer prognosis, Medical Instrumentation, Image processing, and Microprocessors.